INFORMATION TO USERS

This manuscript has been reproduced from the microfilm master. UMI films the text directly from the original or copy submitted. Thus, some thesis and dissertation copies are in typewriter face, while others may be from any type of computer printer.

The quality of this reproduction is dependent upon the quality of the copy submitted. Broken or indistinct print, colored or poor quality illustrations and photographs, print bleedthrough, substandard margins, and improper alignment can adversely affect reproduction.

In the unlikely event that the author did not send UMI a complete manuscript and there are missing pages, these will be noted. Also, if unauthorized copyright material had to be removed, a note will indicate the deletion.

Oversize materials (e.g., maps, drawings, charts) are reproduced by sectioning the original, beginning at the upper left-hand corner and continuing from left to right in equal sections with small overlaps.

ProQuest Information and Learning
300 North Zeeb Road, Ann Arbor, MI 48106-1346 USA
800-521-0600

Muon Spin Relaxation Measurements of the Magnetic System with Itinerant Electrons in MnSi

IOANA M. GAT

SUBMITTED IN PARTIAL FULFILLMENT OF THE
REQUIREMENTS FOR THE DEGREE
OF DOCTOR OF PHILOSOPHY
IN THE GRADUATE SCHOOL OF ARTS AND SCIENCES

COLUMBIA UNIVERSITY

2003

UMI Number: 3095580

UMI Microform 3095580

ProQuest Information and Learning Company
300 North Zeeb Road
P.O. Box 1346
Ann Arbor, MI 48106-1346

Abstract

Muon Spin Relaxation Measurements of the Magnetic System with Itinerant Electrons in MnSi

Ioana M. Gat

This dissertation presents a detailed μSR study of MnSi, a magnetic system with itinerant electrons. The magnetic metals have received a considerable amount of attention from theorists as well as experimentalists in the last 30 years. The conduction band electrons, which are the *d*-band electrons in most of the cases, are responsible for magnetism in these systems. The degree of itinerancy of the electrons, or their atomic character, strongly affects the magnetic properties. It has been shown by comprehensive studies on numerous materials that as the itinerancy of the electrons is increasing, the critical temperature of the magnetic transition and the value of the ordered magnetic moment at T = 0 K are decreasing. In the most itinerant limit, the system does not order down to the lowest temperature, becoming a correlated paramagnet. At present, the theory which is most successful in ex-

plaining the behavior of the itinerant magnets is the Self Consistent Renormalization theory by Dr. Toru Moryia and his collaborators.

The technique we used for the present study is muon spin rotation and relaxation (μSR). This dissertation contains a review of the μSR technique, as well as a general description of the magnets with itinerant electrons, with an emphasis on the MnSi system. A detailed analysis of our findings and the relevant facts supporting the SCR theory are presented. Also, we make an important point to explain when the SCR theory becomes inappropriate for interpreting our results, considering the special helical magnetic structure of the MnSi system.

Contents

List of Figures

Acknowledgements

I would like to thank especially to my advisor, Prof. Yasutomo Uemura, for his support and encouragement during my years of study at Columbia. I am really grateful to benefit from his knowledge and intuition of the physics phenomena studied. As a graduate student in his group, I had the occasion to work together with recognized scientists, such as Prof. Graeme Luke, from McMaster University, and Dr. Toshimitsu Ito, form Japan. I have learned from them a good amount about the μSR technique and the special features encountered in the data analysis. I also got acquainted with many modern research issues relevant to the scientific community.

I would like to thank Prof. Yuri Sushko, from the University of Kentucky, for lending us the high pressure cell, which we used for a good part of our experiments. He is a dedicated researcher and his determination helped us make our original μSR experiments under pressure successful. I wish to thank Dr. Gen Shirane, from the Brookhaven National Laboratory, who kindly lent us a single crystal of MnSi. His

support came at the right time, after performing experiments with ambiguous results, on samples of less quality. I am also really thankful for having the support of the μSR group at TRIUMF, especially of Bassam Hitti, Syd Kreitzman and Mel Good.

I would like to thank Michael Larkin, my former colleague at Columbia, for helping me overcome the difficulties of adjusting to the new environment when I arrived in the group. I received a good amount of help from him while learning about the μSR technique and the analysis of the μSR data. He was also most involved with the experiments we performed on the MnSi system. I really appreciate his interest in the technical and scientific issues raised by my thesis subject. I also wish to thank Dr. Oleg Tchernyshyov, from Johns Hopkins University, and Dr. A. Millis, from Columbia University, for the delightful and enlightening discussions on the nature of magnetism in MnSi.

I am also grateful for having the occasion to collaborate with Kenji Kojima, former graduate student in the group, and Atsuko Fukaya, former researcher in our group. I am really fortunate to receive their advise and their help in acquiring a good understanding of the physics

behind our experiments.

I would also like to thank my colleagues from Columbia, Peter Russo and Andrei Savici, for participating in all the experiments we performed on MnSi. A special thank is dedicated to Peter for having the patience to read my thesis and to suggest improvements. I am also indebted to my colleagues at McMaster University, Pavlos Kyriakou, Chris Wiebe and Martin Rovers, for being helpful and supportive during this entire time.

I would like to thank Prof. Allan Blaer, for encouraging me and advising me in my academic career. He is the best person in the Physics Department to discuss any issue related to the students life and performance. I really appreciate his wisdom, especially as an international student.

During my years of studies at Columbia I had the occasion to teach numerous recitations and laboratory sessions. I especially wish to thank Prof. Morgan May and Prof. Sven Hartmann, from whom I learned to enjoy teaching physics and working together with the students.

On a personal level, I wish to thank my husband, Catalin, and my family, especially my sister and my parents, for their continuous encouragement and support, and for designing for me a model of the person and the professional that I would like to be.

To my family.

1 Theoretical studies of the magnetic systems with itinerant electrons [1]

1.1 Introduction

The problem of magnetism has always been a subject of interest and controversy. The magnetic systems in which electron-electron correlations play an important role, such as magnets with itinerant electrons, have received a considerable amount of attention in the last 30 years. They exhibit very special properties, which were hard to explain in the frame of the existent theories. For example, systems such as $Mn_{0.2}Cr_{0.8}Sb$ and $FePd_{1.6}Pt_{1.4}$ exhibit coexistent ferromagnetic and antiferromagnetic phases. In systems such as Mn_2Sb, transitions between the ferromagnetic and the antiferromagnetic phases were discovered. Other systems such as $ZrZn_2$ show coexistence of superconductivity and magnetism under high pressures, when the critical temperature of the ferromagnetic transition is considerably reduced [2].

[1] This review is inspired from the work of Dr. Toru Moriya, "Spin Fluctuations in Itinerant Electron Magnetism" [1].

1.2 Classical theories of magnetism

The theory of magnetism started with the concept of localized magnetic moments. Using this concept, Langevin [3] predicted the Curie law of paramagnetism for systems with noninteracting local moments. The temperature dependent magnetic susceptibility is given by:

$$\chi = \frac{C}{T}, \quad \text{with} \quad C = \frac{N_0 m^2}{3k_B}. \tag{1}$$

C is the Curie constant and depends on N_0, the number of atoms in the system considered, and m, the magnetic moment/atom.

Subsequently, the occurrence of ferromagnetism in a system of interacting magnetic moments is explained by the Langevin-Weiss theory [4]. The average effect of the interaction between the moments is to generate a mean molecular field $\Gamma < \mathbf{m} >$. At temperatures below the critical temperature, $T_c = m^2\Gamma/3k_B$, the system is in a ferromagnetic state. Above the critical temperature the magnetic susceptibility obeys a Curie-Weiss law:

$$\chi = \frac{C}{T - T_c}. \tag{2}$$

Figure 1 shows the temperature dependence of the magnetization

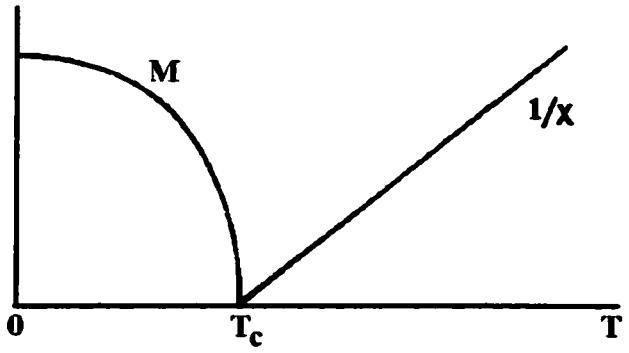

Figure 1: Temperature dependence of magnetization and of the inverse magnetic susceptibility according to Weiss theory [1].

and of the inverse susceptibility, as commonly observed in ferromagnets.

These theories describe the essential properties of ferromagnets both below and above the critical temperature, but there are two difficulties intrinsic to the classical theory of physics. Firstly, it is difficult to classically justify the existence of a magnetic moment of constant magnitude. Also, the Bohr van Leeven theorem [5] shows the absence of magnetism within purely classical statistics. Secondly, the magnitude of the Weiss molecular field, as determined from the dipole-dipole interaction, is inconsistent with the value calculated from T_c.

Both of the above theoretical descriptions are improved by using the principles of quantum mechanics. An electron bound in an atom

has quantized orbital angular momentum, $\hbar\mathbf{l}$, and spin, $\hbar\mathbf{s}$, where $\hbar$ is Planck's constant. The atom's magnetic moment is also quantized in units of Bohr magnetons, $\mathbf{m} = \mu_B(\mathbf{l} + 2\mathbf{s})$, with $\mu_B = e\hbar/2mc$. The total angular momentum of the atom and the total magnetic moment are obtained from $\mathbf{J} = \mathbf{L} + \mathbf{S}$ and $\mathbf{M} = \mu_B(\mathbf{L} + 2\mathbf{S})$, where $\mathbf{L}$ and $\mathbf{S}$ are given by the Russel-Saunders scheme in most of the cases: $\mathbf{L} = \sum_i \mathbf{l}$ and $\mathbf{S} = \sum_i \mathbf{s}$. The eigenstates of the atom are determined by the Hund rules. If the lowest energy state is well separated from the others, one can redefine the total magnetic moment as:

$$\mathbf{M} = g_J \mu_B \mathbf{J}, \tag{3}$$

where g_J is the gyromagnetic Lande factor.

By applying quantum statistical mechanics to a system of N_0 non-interacting localized magnetic moments, a quantum mechanical counterpart for the Langevin theory is obtained. The Curie law for the magnetic susceptibility is rewritten as:

$$\chi = \frac{C}{T}, \quad \text{with} \quad C = \frac{N_0 g_J^2 \mu_B^2 J(J+1)}{3k_B}. \tag{4}$$

The ferromagnetic state of a system with localized magnetic mo-

ments can be described in a frame of models such as the Heisenberg model [6]. The origin of the Weiss molecular field was attributed by Heisenberg to the exchange interaction between spins. The corresponding Hamiltonian is $H = -\sum_{j,l} J_{jl}(\mathbf{S}_j \cdot \mathbf{S}_l)$, where j, l specify atomic sites in the crystal and J_{jl} is the inter-atomic exchange interaction constant. The mean molecular field takes the expression: $\mathbf{H}_{exch} = 2(g\mu_B)^{-1} \sum_l J_{jl} < \mathbf{S}_l >$, where g is the gyromagnetic ratio. The Curie temperature can be calculated from:

$$T_c = \frac{2J(0)S(S+1)}{3k_B}, \tag{5}$$

where $J(0) = \sum_l J_{jl}$. The magnetic susceptibility in the paramagnetic state has a Curie-Weiss law dependence on temperature:

$$\chi = \frac{C}{T - T_c}, \quad \text{with} \quad C = \frac{N_0 g^2 \mu_B S(S+1)}{3k_B}. \tag{6}$$

The above pictures work well for the case of magnetic systems with localized moments, such as the magnetic insulators or the rare earth compounds. But the Heisenberg model in this simple form does not describe the ferromagnetic transition metals. Generally speaking, the s or p electrons are responsible for the crystal bonding, while the f or

d electrons are responsible for the magnetic properties. In the case of the rare earth atoms, for example, the $4f$ electrons do not alter their atomic state much at the formation of the crystal and the total angular momentum, **J**, is a good quantum number. The same can be stated of the localized d electrons in the magnetic insulators. On the other hand, in the case of the magnetic systems with itinerant electrons like the transition metals, the atomic spin is not well defined and the problem of magnetism must be solved using a different approach [1].

1.3 Particularities of magnets with itinerant electrons

System	x	$p_{eff}(\mu_B)$	$p_s(\mu_B)$	p_{eff}/p_s	$T_c(K)$	$T_0(K)$	T_c/T_0
Ni_3Al		1.3	0.075	17.3	41.5	3590	0.0116
Sc_3In		0.66	0.045	14.7	5.5	565	0.0097
$ZrZn_2$		1.44	0.12	12.0	17	321	0.053
$ZrZn_{1.9}$		1.57	0.16	9.8	26	400	0.065
MnSi		2.2	0.4	5.3	30	231	0.13
Au_4V		1.48	0.41	3.62	44	259	0.17
Ni_xPt_{1-x}	.429	1.59	0.051	31.2	23	2160	0.0106
	.452	1.59	0.104	15.3	54	2160	0.025
	.476	1.59	0.143	11.1	74	2160	0.034
	.502	1.59	0.179	8.89	100	2160	0.046

Table 1. Examples of itinerant magnetic systems [7].

Table 1 summarizes some of the features of the magnets with itinerant electrons. These systems have rather low critical temperatures, and, in the paramagnetic state, they obey only an approximate Curie-Weiss law. In the most itinerant limit, the system remains paramag-

netic at $T = 0$ K. The magnetic moment in the paramagnetic state formally derived from the Curie constant, p_{eff}, and the ordered moment at $T = 0$ K, p_s, are independent of each other. As the itinerancy of the electron system in a ferromagnet increases, the ratio p_{eff}/p_s strongly increases [8], as opposed to the case of magnetic systems with localized moments such as Gd or EuO, shown in Table 2. The ratio between T_c, the critical temperature, and T_0, temperature which characterizes the energy width of the dynamical spin fluctuation spectrum, $\chi(\omega, q)$, is decreasing as the itinerancy of the system increases.

System	$p_{eff}(\mu_B)$	$p_s(\mu_B)$	p_{eff}/p_s	$T_c(K)$
Gd	7.13	7.05	1.01	289
EuO	7	7	1.0	77

Table 2. Examples of magnets with localized magnetic moments [8].

The difference between the itinerant magnets and the magnets with localized moments becomes more obvious on the Rhodes-Wohlfarth plot [8], the plot of p_{eff}/p_s as a function of T_c shown in Fig. 2.

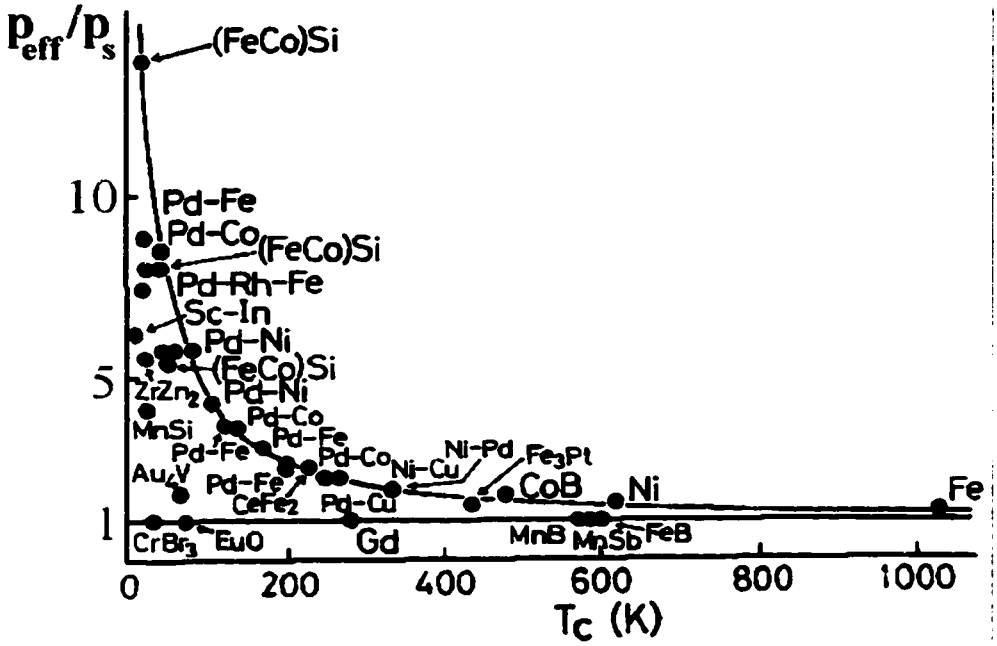

Figure 2: The Rhodes Wohlfarth plot, showing p_{eff}/p_s as a function of the Curie temperature [1].

1.4 Theories of itinerant electron magnetism

In the case of a normal metal, the electron - electron correlations suppress ferromagnetism, according to Wigner [9]. In view of this, one expects that the itinerant electron magnetism is related, to some extent, to the atomic character of the *d*-band electrons and the intra-atomic interactions.

The first model to deal with the problem of itinerant electron magnetism was the Slater model [10], which discusses the magnetic ground states of Ni, by taking into account only the intra-atomic exchange

interaction. The free energy of a system is written as the sum of the kinetic and exchange energies: $E = E_{kin} + E_{exch}$. The exchange energy between the Bloch d-band electrons is $I = J/N_0$, with J the average of the intra-atomic exchange energy and N_0 the number of atoms in the crystal:

$$E_{exch} = \frac{1}{4} I N^2 - I M^2. \tag{7}$$

$N = N_\downarrow + N_\uparrow$, N_σ is the number of electrons with spin σ, and $M = \frac{1}{2}(N_\downarrow - N_\uparrow)$ the magnetization in units of $2\mu_B$.

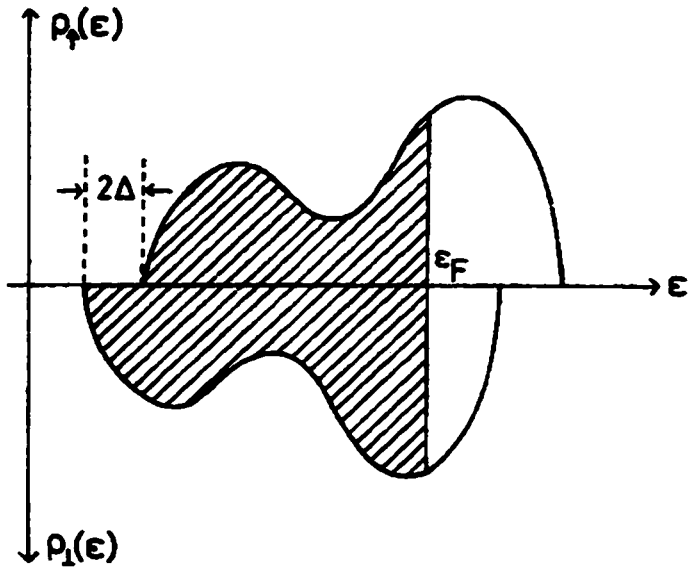

Figure 3: The exchange splitting between the up- and down-spin bands. The shaded area is occupied by electrons [1].

The kinetic energy is derived as a sum over the kinetic energies of the spin up and spin down electrons up to the Fermi level, as shown

in Fig. 3 and it depends on Δ, the exchange splitting of the up- and down-spin bands, and, therefore, on the magnetization.

The total energy becomes a function of the magnetization and particularities of the band structure:

$$E = \frac{1}{\rho}(1 - I\rho)M^2 + \frac{1}{4\rho^3}F_1M^4 + ..., \tag{8}$$

where ρ is the density of states at the Fermi level and F_1 depends on ρ and its first and second order derivatives. The condition for the appearance of feromagnetism, called the Stoner condition for reasons which will appear obvious later, is $\alpha_0 = I\rho(\epsilon_F) > 1$. The magnetization is determined from $M = \rho[2(\alpha_0 - 1)/F_1]^{1/2}$ for $F_1 > 0$. This explains the existence of materials with a magnetic moment/atom different than integral multiples of the Bohr magneton, μ_B.

The theory also predicts the existence of systems with very similar properties as those of the itinerant ferromagnets but which do not become ferromagnetic down to 0 K. They are called nearly ferromagnetic metals, and for these systems, α_0 is slightly less than 1. Their paramagnetic susceptibility at 0 K is enhanced compared to the Pauli

magnetic susceptibility of normal metals with the Stoner enhancement factor, $1/(1-\alpha_0)$:

$$\chi = \frac{1}{(1-\alpha_0)} \frac{\rho(\epsilon_F)}{2}. \tag{9}$$

The extension of the Slater model at higher temperatures is called the Stoner model, or generically, the Slater-Stoner model. There are various versions of the model, depending on the system (ferromagnetic, antiferromagnetic or systems showing helical spin density waves) and the degree of complexity desired. For example, one of the approaches is to calculate the free energy of a ferromagnetic system starting from the Hubbard Hamiltonian:

$$\begin{aligned} H &= \Sigma_{j,l} \Sigma_\sigma \, t_{jl} a^\dagger_{j\sigma} a_{l\sigma} + U \Sigma_j \, n_{j\uparrow} n_{j\downarrow} \\ &= \Sigma_k \Sigma_\sigma \, \epsilon(\mathbf{k}) a^\dagger_{k\sigma} a_{k\sigma} + \\ &+ I \sum_q \sum_k \sum_{k'} a^\dagger_{k+q\uparrow} a^\dagger_{k'-q\downarrow} a_{k'\downarrow} a_{k\uparrow}, \end{aligned} \tag{10}$$

where $a^\dagger_{j\sigma}$ and $a_{l\sigma}$ are the creation and annihilation operators for electrons with spin σ at the sites j and l, respectively, t_{jl} are the transfer energies between the sites j and l, and $\epsilon(\mathbf{k})$ is the band dispersion. U is the effective on-site Coulomb energy ($I = U/N_0$), and the inter-atomic

terms and the degeneracy of the band are neglected.

The Hartree Fock approximation for this hamiltonian gives the free energy:

$$F_0(M,T) = F_0(0,T) + \frac{1}{2\chi_0(T)}M^2 + \frac{g(T)}{4}M^4 + ..., \qquad (11)$$

where $\chi_0(T) = \frac{1}{2}\rho(\epsilon_0)[1 - (\pi^2/6)RT^2]$ is the temperature dependent Pauli susceptibility, $g(T) = F_1/[\rho(\epsilon_0)]^3[1 + (\pi^2/6)R_1T^2]$ and the constants R, F_1, R_1 depend on the density of states at the Fermi level and its derivatives: $\rho, \rho', \rho'', \rho''', \rho^{(4)}$.

The condition for appearance of ferromagnetism is the Stoner condition: $\alpha_0 = I\rho(\epsilon_F) > 1$. The Curie temperature and the magnetization at $T = 0$ can be calculated with the formulas: $T_c = [6(\alpha_0 - 1)/\pi^2\alpha_0 R]^{1/2}$ and $M(0) = \rho[2(\alpha_0 - 1)/F_1]^{1/2}$, respectively. The magnetization for small values takes the form $M(T) = M(0)[1 - (T/T_c)^2]^{1/2}$, which for low temperature translates into $M(0) - M(T) \propto T^2$. The magnetic susceptibility at temperatures above T_c is derived from:

$$\frac{1}{\chi(T)} = \frac{1}{\chi_0(T)} - \frac{1}{\chi_0(T_c)} \text{ or } \frac{1}{\chi(T)} = \frac{\pi^2}{3\alpha_0}IR(T^2 - T_c^2). \qquad (12)$$

The most obvious drawbacks of the theory are that it fails to explain

the Curie-Weiss-like paramagnetic susceptibility, and that the calculated T_c's are systematically higher than the experimental ones. For example, the calculated values of the critical temperatures for Fe, Co and Ni are 5000 K, 4000 K and 2900 K, respectively, while the real T_c's are 1040 K, 1390 K and 630 K. The dependence of the magnetization on temperature, $M(0) - M(T) \propto T^2$, also contradicts the experimental results on Fe or Ni, for which it was found that $M(0) - M(T) \propto T^{3/2}$.

In the Mean-Field or Hartree-Fock theory of itinerant electron magnetism, a thermal spin-flip excitation of an electron across the Fermi level is considered, and an electron and the corresponding hole thus produced are assumed to move independently in a common static mean field. The thermal excitation is usually underestimated. The Dynamical Mean Field theory of the spin fluctuation takes into account the elementary excitations from the ground state and the coupling between them through the exchange interaction, giving rise to exchange-enhanced spin density fluctuations, including spin waves.

Figure 4 shows a schematic view of a ferromagnetic ground state, with the spin up and spin down electron seas. A magnetic excitation

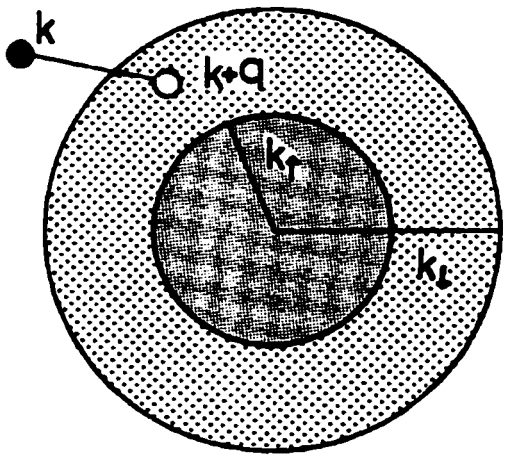

Figure 4: Fermi spheres for ↓ and ↑ electrons and an electron-hole pair excitation with momentum q [1].

from the ground state is equivalent to the formation of an electron-hole pair, which evolves under the influence of a magnetic field or due to the exchange coupling. The quantum state of the system can be represented with the wave function:

$$\Psi_0 = \prod_{k<k_\uparrow} a^\dagger_{k\uparrow} \prod_{k<k_\downarrow} a_{k\downarrow} \Psi_{vac}, \tag{13}$$

where Ψ_{vac} is the non-excited state, $a^\dagger_{k\uparrow}$ is the creation operator for the electron with momentum k, and $a_{k\downarrow}$ is the creation operator for the hole with momentum k and spin down. $k_\uparrow$ and $k_\downarrow$ are the Fermi radii of the majority (down) and minority (up) spin electrons.

The magnetic excitation with momentum q consists of an electron with wave-vector $k + q$ excited across the Fermi level in a state with

wave-vector k. It can be represented mathematically as $S_+(k,q) = a^\dagger_{k\uparrow}a_{k+q\downarrow}$. One can study the equation of motion of the electron-hole pair using the Hubbard Hamiltonian, for brevity, and an additional oscillating magnetic field, $H_{ext} = \Sigma_{k'} S_-(k',-q)h_+(q)$:

$$i\dot{S}_+(k,q) = [S_+(k,q), H + H_{ext}] =$$

$$= [\epsilon_{k+q} - \epsilon_k - I\,\Sigma_{k'}(n_{k'\downarrow} - n_{k'\uparrow})]S_+(k,q) +$$

$$+ I(n_{k+q\downarrow} - n_{k\uparrow})\,\Sigma'_{q'}\,S_+(k+q',q) -$$

$$- I\,\Sigma'_{q'}\,\Sigma_{k'}[(1-\delta_{kk'})a^\dagger_{k\uparrow}a_{k'\uparrow}a^\dagger_{k'+q'\uparrow}a_{k+q+q'\uparrow} -$$

$$- (1-\delta_{k'-q',k+q})a^\dagger_{k'-q'\downarrow}a_{k+q\downarrow}a^\dagger_{k+q'\uparrow}a_{k'\downarrow}] +$$

$$+ (n_{k\uparrow} - n_{k+q\downarrow})h_+(q) \qquad (14)$$

The first three terms on the right hand side represent the diagonal part of the Hamiltonian, the scattering of the electron-hole pair through the exchange interaction, with the conserved momentum transfer q, and the scattering without conservation of the momentum transfer, respectively. The third term was not taken in account in this model. The diagonal part of the Hamiltonian gives the kinetic energy and the mean field energy of the electron hole pair. Only this term was considered in the Stoner theory based on HFA, the energy spectrum

of the Stoner excitation being expressed as:

$$\omega_{Stoner}(k,q) = 2\Delta + \epsilon_k - \epsilon_{k+q}, \tag{15}$$

where 2Δ is the exchange splitting of the band.

Taking the statistical averages for $S_+(k,q)$ and $n_{k\sigma}$, one obtains:

$$\begin{aligned}(\epsilon_k - \epsilon_{k+q} + 2\Delta - \omega) < S_+(k,q) >= \\ =< n_{k+q\downarrow} - n_{k\uparrow} > [I < S_+(q) > -h_+(q)],\end{aligned} \tag{16}$$

where $S_+(q) = \Sigma_k S_+(k,q)$ is the Fourier q component of the spin density $S_x(r) + \mathrm{i}S_y(r)$. $I < S_+(q)$ is the equivalent of an oscillating molecular field, therefore this approximation is called the dynamical mean-field approximation or the Random-Phase Approximation.

The intensity of the excitation with the wave-vector transfer q and the energy ω is given by the imaginary part of the dynamical susceptibility. As seen in Figure 5, the spin fluctuation spectrum is changed dramatically in the presence of the coupling between the spin excitations as compared to the Stoner excitations, obtained by ignoring the exchange enhancement.

Assuming that $h_+(q)$ oscillates in time as $\exp(i\omega t)$, one obtains the dynamical susceptibility in the Hartree-Fock approximation as:

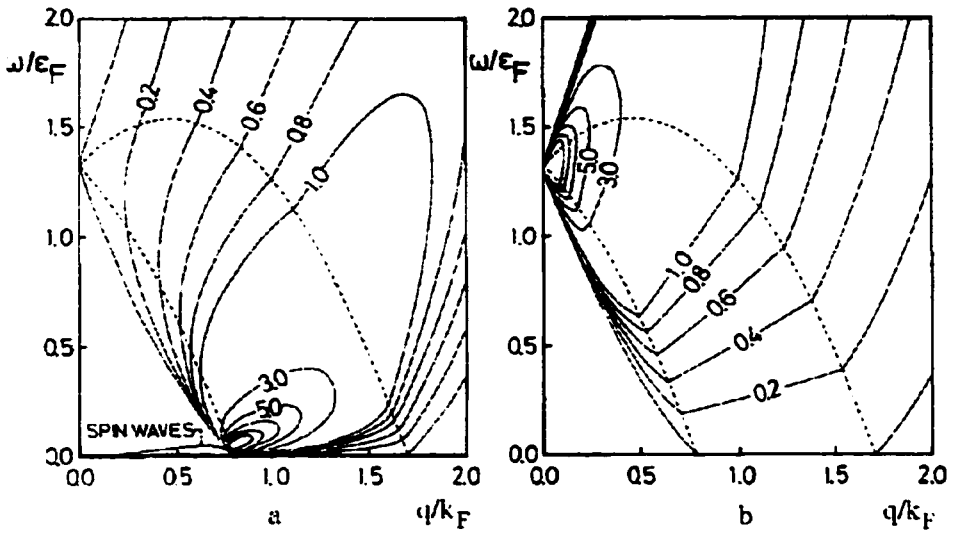

Figure 5: (a) Intensity contours of the imaginary part of the RPA transverse dynamical susceptibility in a ferromagnetic electron gas. The spin wave dispersion is also shown. (b) Intensity contours for the Stoner excitations (no exchange enhancement) [1].

$$\chi^{+-}_{\Delta 0}(q,\omega) = \frac{<S_+(q)>}{h_+(q)}$$

$$\text{or } \chi^{+-}_{\Delta 0}(q,\omega) = \sum_k \frac{< n_{k+q\downarrow} - n_{k\uparrow} >}{\epsilon_k - \epsilon_{k+q} + 2\Delta - \omega}. \tag{17}$$

In the Random-Phase Approximation (RPA) considered, the dynamical susceptibility can be written as:

$$\chi^{+-}_{RPA}(q,\omega) = \frac{\chi^{+-}_{\Delta 0}(q,\omega)}{1 - I\chi^{+-}_{\Delta 0}(q,\omega)} \tag{18}$$

The singularity in the expression of the RPA dynamical susceptibility is an indication of the presence of the spin wave excitations. The dispersion equation for the spin waves is determined from:

$$1 - IRe\chi^{+-}_{\Delta 0}(q, \omega_q) = 0. \tag{19}$$

The static transverse susceptibility is obtained in the limit $q \to 0$ and $\omega \to 0$ from $1 - I\chi^{+-}_{\Delta 0}(0,0) = 0$, with which one can rewrite the spin wave dispersion relation as $\chi^{+-}_{\Delta 0}(0,0) - Re\chi^{+-}_{\Delta 0}(q, \omega_q) = 0$.

Another success of the theory is that it predicts correctly the enhancement of the spin fluctuations near the critical temperature or in the nearly ferromagnetic metals.

According to the experiment, one expects that the fluctuation spectrum is enhanced around the small wave-vector, $q \to 0$, and small energy, $\frac{\omega}{q} \to 0$ region in the q space. By expanding the dynamical susceptibility in powers of q and $\frac{\omega}{q}$, one can write the Hartree-Fock susceptibility as:

$$f_{\Delta 0}(q, \omega) = \frac{\chi^{+-}_{\Delta 0}(q, \omega)}{\chi^{+-}_{\Delta 0}(0,0)} = 1 - Aq^2 - B\frac{\omega^2}{q} + ... + iC\frac{\omega}{q}, \tag{20}$$

where the coefficients A, B and C are dependent on the band structure properties. The Random Phase Approximation dynamical susceptibility in the paramagnetic state ($\Delta = 0$) takes the following expression:

$$f_{RPA}(q,\omega) = \frac{f_{00}(q,\omega)}{1-\alpha f_{00}(q,\omega)}, \tag{21}$$

with $\alpha = I\chi_{00}^{+-}(0,0)$ and $\Delta = 0$. The magnetic susceptibility is enhanced in the region $q \to 0$ and $\frac{\omega}{q} \to 0$ of the q space when α is close to 1, near the magnetic-nonmagnetic transition. Figure 6 shows this effect as a function of the exchange enhancement factor and wave-vector [11].

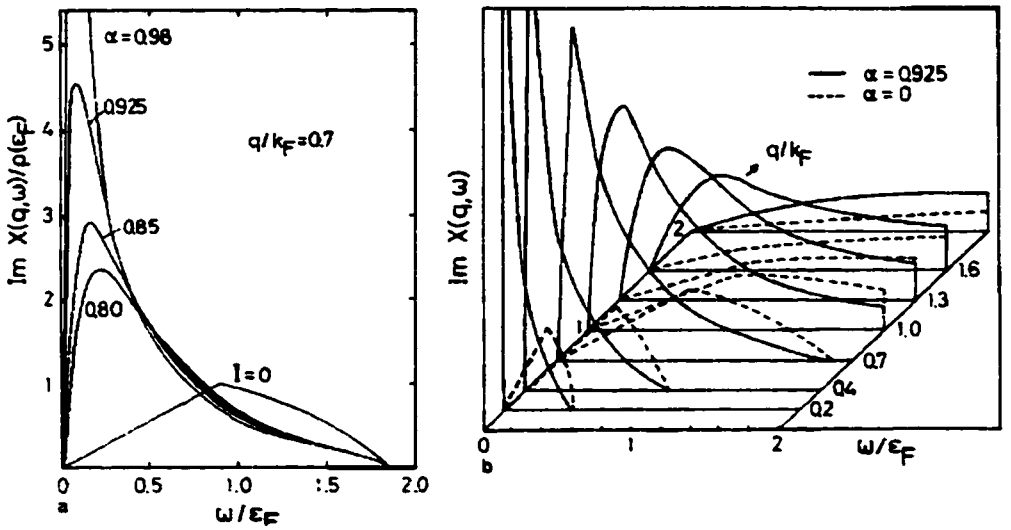

Figure 6: Imaginary part of the exchange-enhanced dynamical susceptibility for an electron gas model; (a) for various values of exchange enhancement factor; (b) for various values of wave-vector [1].

The HFA or the band theory calculates the ground states well, and the RPA theory is successful in describing the elementary excitation from the ground state. However, both of these approaches are not

satisfactory at finite temperatures.

1.5 The Self Consistent Renormalization Theory

The Self Consistent Renormalization (SCR) theory developed by T. Moriya and his coworkers set the framework for interpreting most of the experimental results accumulated up to now [1]. The renormalization method used by SCR takes into account the effect of spin fluctuations on macroscopic properties such as the ordered moment size and the magnetic susceptibility. Through a self consistent treatment, the dynamical susceptibility $\chi(q, \omega)$ and the free energy are calculated at the same time, with the requirement that the static long wavelength limit of the dynamical susceptibility agrees with the one calculated from the renormalized free energy. The theory correctly predicts the critical temperature of the magnetic-nonmagnetic and the approximate Curie-Weiss like dependence of the magnetic susceptibility above T_c. The Curie constant depends not on the saturation moment at 0 K but on the band structure. The outcome of neutron scattering or μSR experiments can be interpreted easily in the frame of the SCR theory.

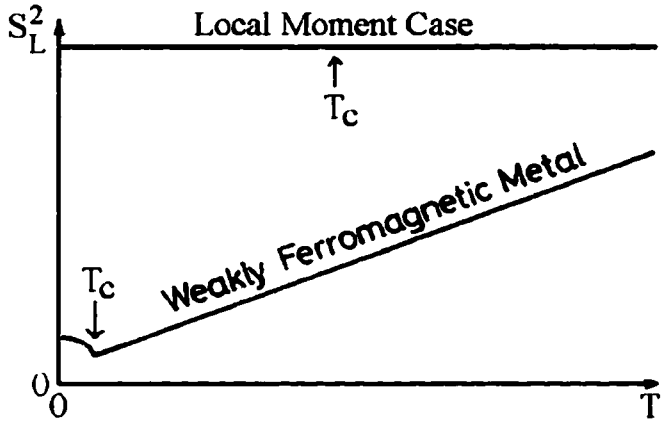

Figure 7: Temperature dependence of the mean-square local amplitude of the spin density S_L^2 in a weakly ferromagnetic metal and in a local moment system [1].

According to SCR, in the case of itinerant systems the magnetic susceptibility obeys a Curie-Weiss law due to a totally different mechanism than the one producing CW law in the magnets with localized magnetic moments. Namely, as the temperature increases, one expects that the spin fluctuation modes with higher energies and higher momenta to become more and more thermally excited. The temperature dependence of the local amplitude of the thermal spin fluctuation, $S_L^2(T)$, is linear, except for a small region around the critical temperature, as shown in Figure 7. $S_L^2(T)$ for the case of magnets with localized moments is shown for comparison. The magnetic susceptibility is related to the amplitude of the thermal spin fluctuations according

to $S_L^2(T) - S_L^2(T_c) = \frac{3}{5gN_0^2}\frac{1}{\chi}$, with $S_L^2(T_c) = \frac{3}{5}(\frac{M(0)}{N_0})^2$, from which the Curie-Weiss law is easily derived.

The purpose of our experiments on MnSi under zero and 8.3 kbar applied pressure was to investigate the ferro-para crossover and the validity of SCR theory with increasing itinerancy. To confirm the predictions of the theory, we performed theoretical calculations which are presented in more detail in chapter 4.3.

2 The MnSi systems

2.1 Main features of the system

Manganese mono-silicide (MnSi) is a magnetic system with itinerant electrons that orders at a temperature $T_c = 29.5$ K in a helical magnetic structure with a long period of 180±3 Å along the <111> axis. The system shows a small ordered moment of 0.4 μ_B per Mn at $T = 0$ K [12]. In a magnetic field, the helical structure becomes progressively more conical, as shown in the field-temperature phase diagram in Fig. 8, without significantly changing its wavelength.

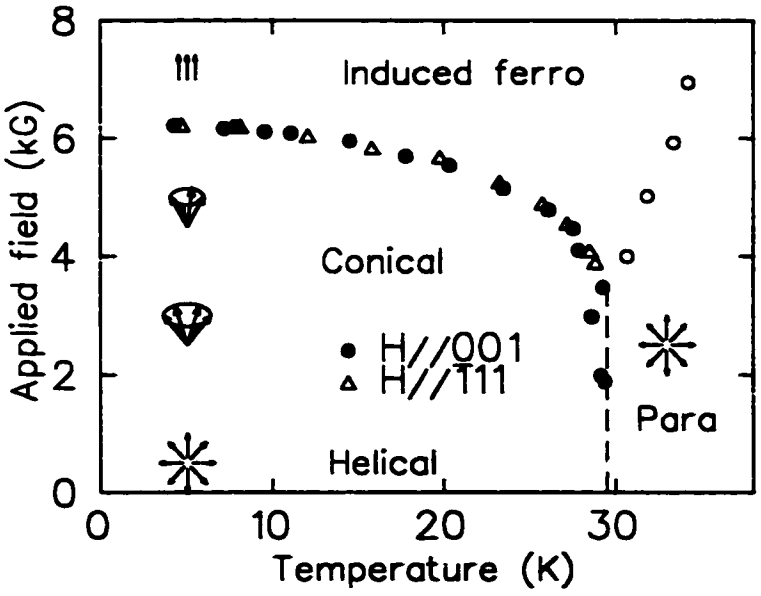

Figure 8: Phase diagram of MnSi at ambient pressure [13].

Depending on the direction of the applied magnetic field, the

helical axis aligns with the applied field at values of the magnetic field from 1500 G to 4000 G [12]. Above 6.2 kG (at 4.2 K), the system behaves like a ferromagnet having a relatively large high field susceptibility [14], as common for ferromagnets with itinerant electrons. In the paramagnetic state, the uniform magnetic susceptibility obeys a Curie-Weiss law up to 400 K [15].

MnSi has been extensively studied as a prototype of itinerant weak ferromagnets which follow predictions of the Self Consistent Renormalization theory, as described in what follows.

2.2 Neutron scattering experiments

As characteristic for the magnetic systems with itinerant electrons close to the ferromagnetic to paramagnetic crossover, strong spin fluctuations persist at a rather high energy scale. For MnSi, this was shown by neutron scattering experiments performed by Y. Ishikawa [16] and his collaborators in 1977. Figure 9 shows the intensity contours for neutron paramagnetic scattering at 33 K, above T_c, and at 270 K. At temperatures close to T_c, the spin fluctuation spectrum ex-

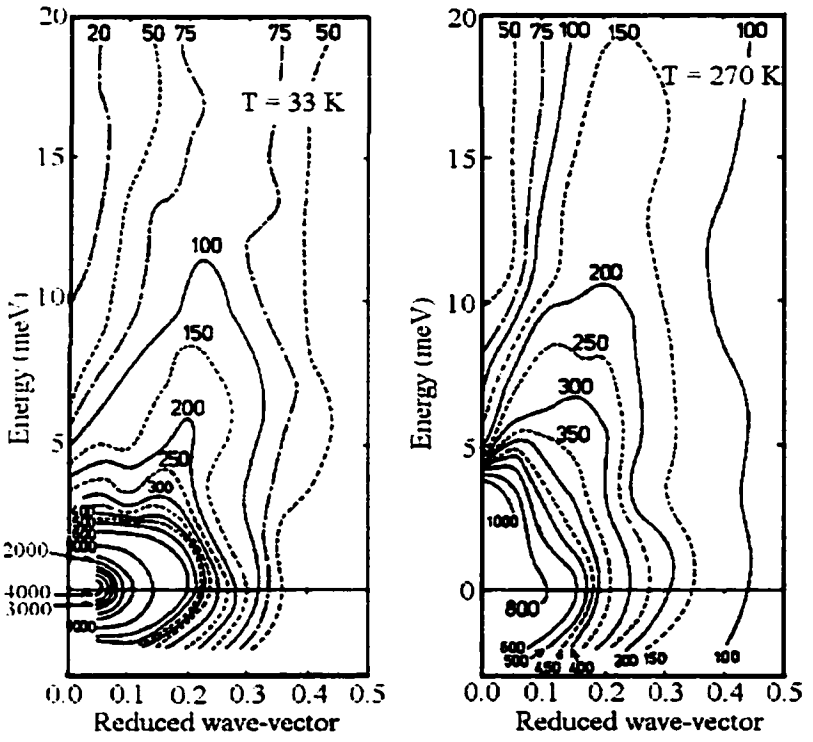

Figure 9: Intensity contours for neutron paramagnetic scattering for MnSi at (a) 33K and (b) 270K [16].

tends to energies scales as high as $10\times T_c$. The small wavevector and low energy components have the highest weight in the spectrum. The main features of the spectrum do not change as the temperature is increased to approximately $10\times T_c$, but spin fluctuations with higher wave-vector are becoming more and more thermally excited.

2.3 μSR experiments

Hayano *et al.* [17] performed muon spin relaxation (μSR) measurements in MnSi and reported a divergence of the spin-lattice relaxation

rate $\frac{1}{T_1}$ observed above T_c in an applied longitudinal field B_L of 700 G, following $T_1 \propto (1 - \frac{T_c}{T})$. Figure 10 presents the T_1 versus $\frac{1}{T}$ plot, and the fit of the data to the above dependence. This is consistent with the prediction of the SCR theory at temperatures above T_c, where the magnetic susceptibility obeys a Curie-Weiss law.

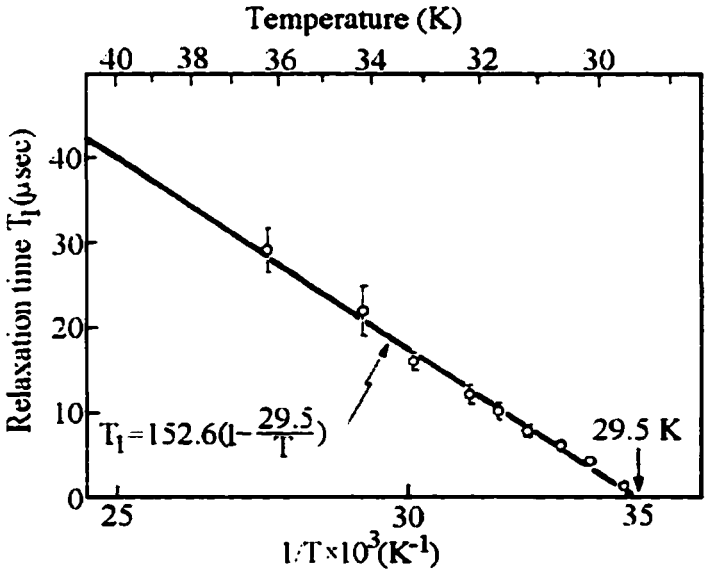

Figure 10: Muon spin relaxation time in MnSi (study on a single crystal sample) [17].

The μSR results above the critical temperature could be compared with the ^{55}Mn NMR scattering results at high temperature. If one assumes that the muon does not change significantly the magnetic environment around the muon site, the following scaling relation between the μSR and NMR relaxation times holds:

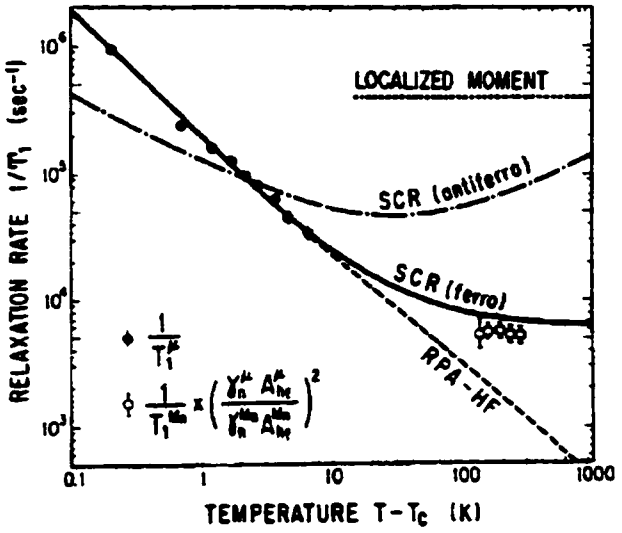

Figure 11: The spin lattice relaxation time T_1 vs $T - T_c$. The full circles are the muon data and the open circles are the Mn data scaled accordingly [17].

$$\frac{1}{T_1} \propto \gamma_N^2 A_{hf}^2 \rightarrow \frac{1}{T_1^\mu} \approx \frac{1}{T_1^{Mn}} \times (\frac{\gamma_N^\mu A_{hf}^\mu}{\gamma_N^{Mn} A_{hf}^{Mn}})^2. \tag{22}$$

Figure 11 shows the plot of the spin lattice relaxation time T_1 vs $T-T_c$. The ^{55}Mn NMR data is scaled accordingly. The fit based on the SCR theory for ferromagnetic metals is shown by a solid line, while the Hartree-Fock (Random Phase Approximation) curve is shown by the broken line. The dotted line is the estimate of the localized moment model. The SCR prediction for anti-ferromagnets is also shown for comparison. The SCR theory for ferromagnetic metals gives the best fit to the data. [17].

Kadono *et al.* [18] confirmed Hayano's result in subsequent μSR

studies, which elucidated muon-nuclear double relaxation effects and extended the measurements to the ordered state.

Two precession frequencies have been observed in the ordered state, corresponding to two muon sites with different hyperfine coupling constants. Two muon sites are expected also in the paramagnetic state, but, due to limited statistics, one can not distinguish two relaxation rates. All data in the paramagnetic state has been fit with one relaxation function.

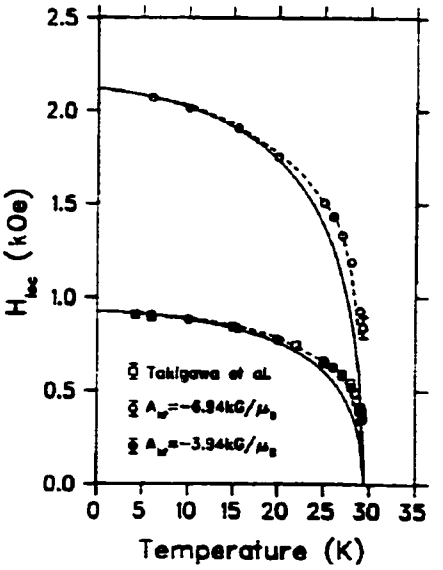

Figure 12: Temperature dependence of the local magnetic fields H_{loc} felt by muons. Previous data are shown as open squares. Solid lines: theoretical calculations of the normalized magnetization $M_Q(T)/M_Q(0)$. Dashed lines: the $M_Q(T)/M_Q(0)$ determined from neutron scattering [18].

The temperature dependence of the internal field is estimated from the muon precession frequency, $\omega = \gamma_\mu B$, as shown in Fig. 12. The

data agrees within the experimental uncertainty with the results of neutron scattering experiments.

2.4 Resistivity and magnetic susceptibility measurements under applied pressure

Recently, Pfleiderer *et al.* [19] found that in applied pressure above $p_c = 14.6$ kbar, MnSi loses static magnetic order and becomes a correlated paramagnet. The crossover from a spin-polarized state to a non-polarized state at low temperature was investigated via high precision measurements of the electrical resistivity and magnetic susceptibility.

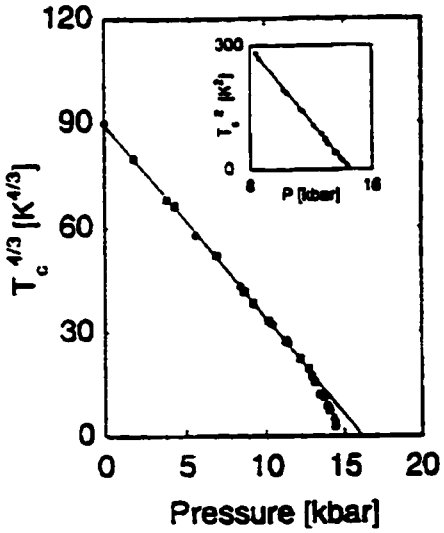

Figure 13: Pressure dependence of the transition temperature. For $p < p^*$ ($\approx$ 12 kbar), $T_c^{4/3} \propto p$, while for $p^* < p < p_c$ ($\approx$ 14.6 kbar), $T_c^2 \propto p$ [19].

It was found that, for $p < p^*$ ($\approx$ 12 kbar), $T_c^{4/3} \propto p$, while for

$p^* < p < p_c$, $T_c^2 \propto p$. p^* corresponds approximately to the pressure where the transition at T_c changes from a second order transition for $p < p^*$ to a first order transition for $p > p^*$. The pressure dependence of the critical temperature is shown in Fig. 13.

Of a considerable interest is the non-Fermi liquid behavior of the resistivity above T_c. For a Fermi liquid in a paramagnetic or weakly polarized state, one expects $\frac{\Delta\rho}{T^2} = \frac{\rho-\rho_0}{T^2}$ to be temperature independent. ρ is the resistivity and ρ_0 is the residual resistivity at T = 0 K. As seen in Fig. 14(a), the system in the paramagnetic state departs from the Fermi liquid behavior. Pfleiderer *et al.* explains the behavior of MnSi near and above p_c in the frame of a model of a marginal Fermi liquid in which the long range effective interaction between quasi-particles is due to the exchange of long-wavelength nearly critical fluctuations in spin density. Figure 14(b) shows the behavior of the magnetic susceptibility as a function of temperature and pressure. For $p > p^* = 12$ kbar, the magnetic susceptibility shows a step at T_c, characteristic for a first order phase transition.

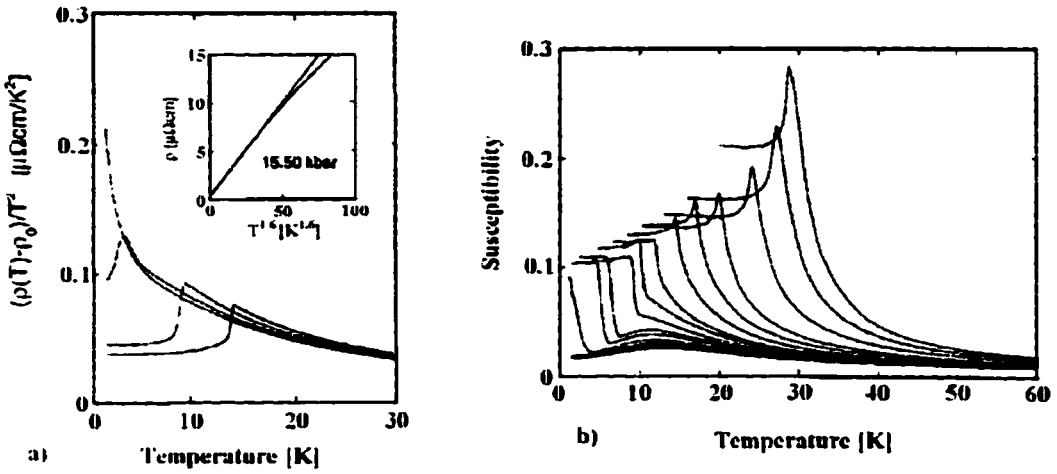

Figure 14: (a) The ratio of $\Delta\rho = \rho - \rho_0$ to T^2 versus temperature at different pressures (10.4, 19.9, 14.3 and 15.5 kbar going up, starting from the bottom curve at left). (b) The magnetic susceptibility versus temperature at different pressures (ambient $\rightarrow$ 16.1 kbar, starting from the top curve at 30 K) [19].

2.5 NMR measurements under pressure

The pressure experiments on MnSi were continued by ^{29}Si NMR [20] and magnetization measurements [21] performed by C. Thessieu *et al.*. The same pressure dependence of the Curie temperature has been obtained as in the above resistivity measurements, as shown in Fig. 15.

The NMR resonance frequency at 1.4 K, also plotted in Fig. 15, shows little pressure dependence and decreases abruptly around p_c. Other NMR experiments performed by the same group show the decrease of the ordered moment right at p_c, as expected for first order

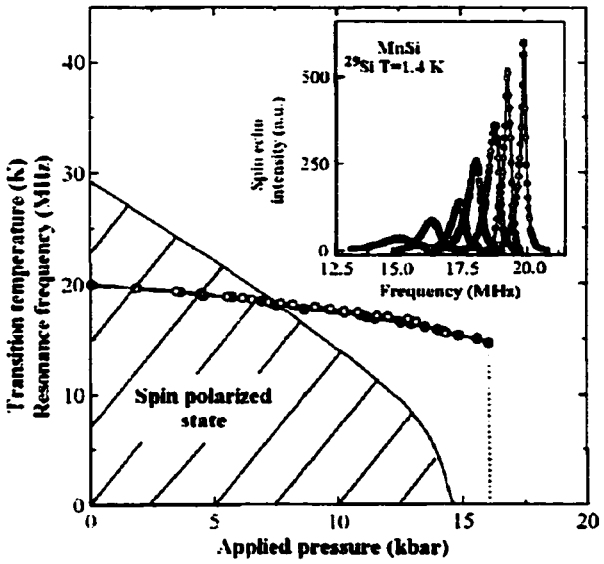

Figure 15: Pressure effect on the Curie temperature T_c (-) and on the resonance frequency f_0 ((•) increasing P and ( ) releasing P). The inset presents the pressure effect on the resonance line of the ^{29}Si nuclei at T = 1.4 K (study on a powdered single crystal) [20].

transitions [22]. The lineshape of the resonance line broadens as the pressure increases through p_c. The magnetization measurements [21] confirmed the very slow dependence of the ordered moment p_s on the applied pressure.

3 The μSR Technique at TRIUMF [2]

3.1 Generalities

The positive muon spin rotation and relaxation technique (μSR) was suggested by experiments trying to show the parity violation in meson decays. Due to the parity non-conservation in the $\pi^+ \rightarrow \mu^+$ decay, it is possible to provide beams of 100 % polarized muons. A polarized muon beam can be stopped in a sample, where the muon spin changes with time under the influence of the local magnetic fields until it decays with an average lifetime of 2.2 μsec according to $\mu^+ \rightarrow e^+ + \nu_e + \bar{\nu}_\mu$. The decay positron is emitted preferentially along the direction of the spin of μ^+ because of the same parity non-conservation. This allows determination of the statistical average of the muon spin polarization as a function of time. The short lifetime of muons limits the applicability of the technique to events visible in the time range from .02 to 10 μsec.

Muons provide a remarkably powerful probe of magnetism in the

[2] All figures of this chapter are taken from the Operation Manual of the Triumf facility.

matter due to the sensitivity of the muon magnetic moment to the local magnetic fields. By determining the time evolution of the muon spin polarization in the magnetic environment inside of a sample, the μSR technique allows detection of static magnetic fields as small as a fraction of a gauss and fluctuating fields on the time scale between 10^{-3} and 10^{-6} seconds.

There are two μSR techniques: Time-Differential (TD-μSR) and Time-Integral (I-μSR). In the case of (TD-μSR) each muon entering the sample starts a clock, and the time and the direction of the decay $e^{\pm}$ are both recorded. The TRIUMF facility provides a continuous muon beam, which requires the muons to be taken one at a time and individual decays correlated with individual muons. If a second muon arrives in the sample within 5 muon lifetimes after the arrival of a first muon, the event is discarded. This imposes a limit on the muon beam rate, which is approximately 30 kμ/sec. The Time Integral μSR makes no correlation between the muon arrival and decay, but counts the number of decays in opposing directions, which allows to use all the muons delivered. TD-μSR is used for all of our experiments.

3.2 Production of the muon beam

The TRIUMF facility is based on a cyclotron capable of accelerating negative hydrogen ions (H^-) to energies up to 520 MeV. The H^- beam is passed through a thin carbon foil which strips off the two electrons. The proton beam resulted is bent out from the cyclotron due to its opposite charge and directed towards the experimental areas. TRIUMF allows the simultaneous extraction of several proton beams of different energies and intensities. The proton beams are directed through the meson production target, usually 1 cm graphite or Beryllium, where they produce pions by nuclear reactions. Pions decay into muons with an average lifetime of 26 nsec. Depending on the purpose of the experiment, one can use the muons which result from the decay of the pions that come at rest at the surface of the production target, called surface muons, or use the muons that result from the "in flight" decay of the high energy pions.

The higher energy pions escape the production target and pass through a quadrupole magnet selecting the pion momentum. Pions with well defined momentum are decaying into muons along the π

decay section, which consists of a series of quadrupole magnets or a superconducting solenoid. The muon momentum is selected by dipole magnets, and it can vary between a range of 20 MeV/c to 100 MeV/c. The resulted muon beam is more than 80 % polarized. The M9B muon channel at TRIUMF specializes in highly energetic muon beams.

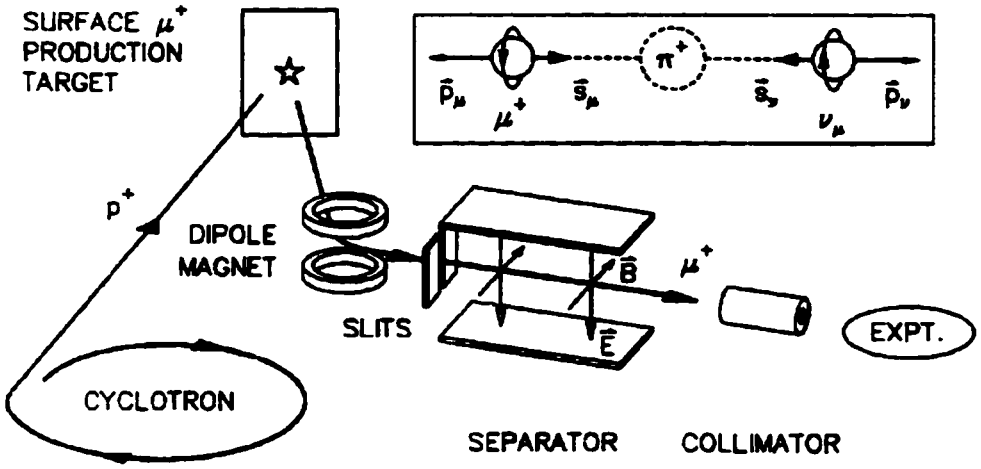

Figure 16: Production of polarized surface muons

Figure 16 shows the schematic view of the beam elements required for the production of the surface muon beam. The surface muons are perfectly polarized opposite to their momentum, which is 29.8 MeV/c. The muon momentum is selected by the use of dipole magnets. This makes sure that the resulting beam has the correct polarization. Quadrupole magnets are used to focus the muon beam. Various slits limit also the momentum range transmitted and the final spot size.

Other charged particles are stripped out using crossed E and B fields in the DC separator. If the magnetic field is high enough, the DC separator can be used to rotate the muon spin perpendicular to the beam direction. The highly collimated muon beam reaches the end of the beam pipe, which is sealed with a thin Kapton or mylar window, and moves toward the experimental area. Before reaching the experiment, the beam passes through a several millimeters large collimator. The M13, M15 and M20 muon channels are designed to produce surface muons.

3.3 Experimental set-up

The experimental set-up is realized by the use of μSR spectrometers and the μSR inserts. A schematic view of the μSR apparatus is presented in Fig. 17.

3.3.1 Spectrometers

The μSR spectrometers are magnets plus an array of counters to detect incoming muons and their decay positrons. The detectors are

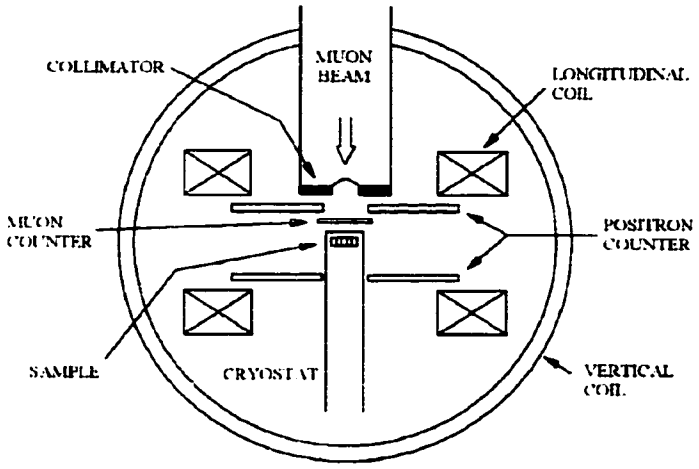

Figure 17: Top view of schematic layout of a μSR apparatus

usually made of plastic scintillators that are connected to photo-tubes through light guides. When a charged particle passes through a detector, the photo-tube will give an electric signal. The muon counter is placed between the sample and the end of the beam line and detects the arrival of an incoming muon. To make sure that the muon reaches the sample, the muon counter is very thin (.25 mm). The positron counters, approximately 1 cm thick, are paired along some specific directions: $\hat{z}$, along the beam, $\hat{x}$, up, perpendicular to the beam and $\hat{y}$, to the right. The main magnet is oriented so that the magnetic field is applied along the beam axis. Other coils provide weaker fields in directions transverse to the beam direction. Depending on the information needed, the positron counters and the magnetic fields are arranged in

one of the longitudinal or transverse field configuration.

3.3.2 Longitudinal field configuration

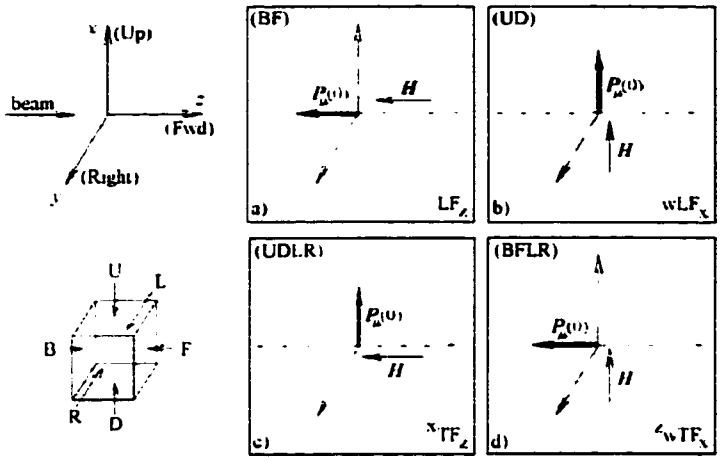

Figure 18: Coordinate system and labelling conventions for surface μSR experiments. a) and b) show possible longitudinal field configurations, with the muon spin polarization and the applied magnetic field along the same direction, indicated by the subscript on the right; c) shows the spin rotated configuration suited for high transverse fields and d) shows the weak transverse field configuration.

In the longitudinal field (LF) configuration (which is suited also for zero field (ZF) measurements) the magnetic field is applied along the initial muon momentum, which coincide with the muon spin direction. The positrons are registered by the forward (F) and backward counters (B) as shown in Fig. 18(a). The muons pass through a small hole in the backward counter, then through the thin muon counter (M). At t = 0 nsec positrons are emitted preferentially in the backward direction.

After enough time, the muon spin looses its polarization, and there is no distinction between the forward and backward directions. The evolution of the component of the muon spin polarization along the beam direction is characterized by the longitudinal relaxation time T_1.

3.3.3 Transverse field configuration

In a transverse field (TF) muon spin rotation experiment a magnetic field is applied perpendicular to the muon spin polarization, causing the spin to precess about it. The technique is used both for measuring the muon precession frequency ($\omega = \gamma_\mu B$, where B is the local field at the muon site) and the rate at which the muon looses phase coherence (T_2 relaxation). Since B can be affected by diamagnetism, paramagnetism, or contact hyperfine interactions with polarized electrons in the medium, B can be different than the external magnetic field applied. The difference is usually the focus of the TF-μSR experiment. There are two possible transverse field configurations. In the configuration shown in Fig. 18(d), a weak magnetic field (maximum 200 G) is applied perpendicular to the muon momentum. The muon spin precesses

around the magnetic field applied until it decays, and the positrons are counted by using forward and backward counters. This technique is not appropriate for higher magnetic fields, which may curve the trajectory of the muon up to the point where it misses the sample. For high fields, the configuration shown in Fig. 18(c) is used. The muon spin is rotated in the DC separator, while the magnetic field is applied along the muon momentum.

3.3.4 Inserts

The μSR inserts consist of cryostats and sample holders. The temperature of the sample can be varied in the range of 2 to 300 K using a He^4 cryostat and between 20 mK and 6 K using a He^3-He^4 dilution refrigerator. For the experiments presented in this thesis, He^4 cryostats have been used. In a He^4 cryostat, the sample is placed at the end of the sample space, next to a mylar window in the cryostat wall facing the beam line. The other end of the sample chamber is connected to a rotary pump, which maintains a very low pressure in the sample space. Close to the sample position, He^4 is passed through

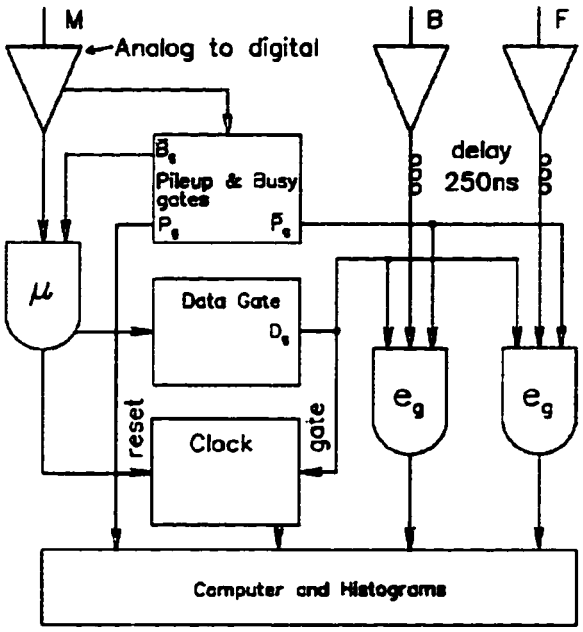

Figure 19: Electronics diagram for recording the data.

a diffuser, where it expands from the high pressure liquid phase into a low pressure gas phase. The diffuser is connected to a liquid He^4 dewar through a capillary with a needle valve. The thermal expansion of He^4 provides the cooling power, which can be controlled by adjusting the needle valve. The temperature of the sample is finely adjusted by two heaters, the diffuser heater and the sample heater. GaAlAs diode thermometers placed very close to the sample are used to measure the sample temperature on a wide temperature range.

3.4 Electronics

The electronic circuits are designed to record the time the muon spent in the sample before it decayed. Raw counter pulses are fed to fast constant fraction discriminators (CFDs) that generate uniform timing pulses if the raw pulse height is above a threshold. Figure 19 shows the electronics diagram for constructing the time histogram. The incoming muon sends a start pulse to a fast "time digitizer", the TDC (Time to Digital Converter) clock, and a data gate (D_g) is opened for a time $t_g \gg \tau_\mu$. It is possible for many muons to enter the sample at about the same time or for a muon to decay before reaching the experimental area and its positron to be mistakenly associated with a muon that arrived in the sample earlier. Additional modules ensure that "second muon" events are rejected. At the arrival of the muon a Pile-up gate (P_g), which is longer than the data gate (D_g) with approximately 500 nsec, is set to "false", a busy gate (B_g) is set to "true" and the data gate is set to "true". If a second muon arrives, the P_g gate is flipped and remains "true" for the rest of the time t_g. Before the arrival of the muon, the B_g gate was set to "false", command which also resets

the number of positrons previously counted, $n = 0$. The condition to accept a positron event (e = "true") and increase n to $n + 1$ is that $\overline{P}_g D_g e$ = "true". The event is registered if when the clock is reset $n = 1$, and P_g = "false".

The procedure described above does not eliminate the background (B) signal due to random triggers, even if only from cosmic rays. To determine B, the best procedure is to delay the signal from the positron counters with several hundred nanoseconds. A good event can then be formed by the muon event, and an "e" event that happened physically before the muon arrival. These events are random noise and the histogram for $t < 0$ provides a measure of the background.

3.5 Reconstructing the muon spin

The positive muon decays according to the relation: $\mu^+ \rightarrow e^+ + \nu_e + \overline{\nu}_\mu$. The decay probability of the muon depends on its spin direction, the direction of e^+ emission and the e^+ energy, $x \equiv \frac{\epsilon_e}{\epsilon_{max}}$ (where $\epsilon_{max} = 52.83$ MeV is the maximum possible energy of the e^+). The higher the energy of the positrons, the more asymmetric the decay probability is.

Figure 20 shows the probability of positron emission integrated over the positron energies.

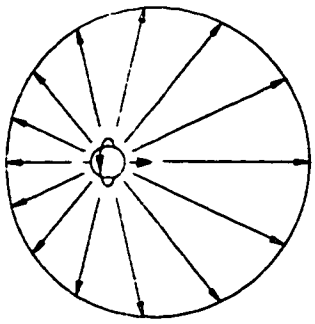

Figure 20: Angular distribution of positrons from muon decay, integrated over energy.

Thus, it is only possible to reconstruct the projection of the muon spin, $S_{\mu,z}(t)$, on one axis, $G_z(t) \equiv < S_{\mu,z}(t) >$. The most convenient experimental set-up is formed by a pair of counters. The same information could be extracted with more difficulty from the time histogram accumulated with a single counter. Figure 21 shows a typical counter arrangement.

The projection of the muon polarization along the z axis is $G_z(t) = cos(\theta(t))$, where θ is the angle made by the muon spin with the counter axis. The time spectra in the two counters can be described by:

$$N_+(t) = B_+ + N^0 \epsilon_+ e^{-t/\tau_\mu}(1 + A_+ G_z(t)),$$

$$N_-(t) = B_- + N^0 \epsilon_- e^{-t/\tau_\mu}(1 - A_- G_z(t)), \qquad (23)$$

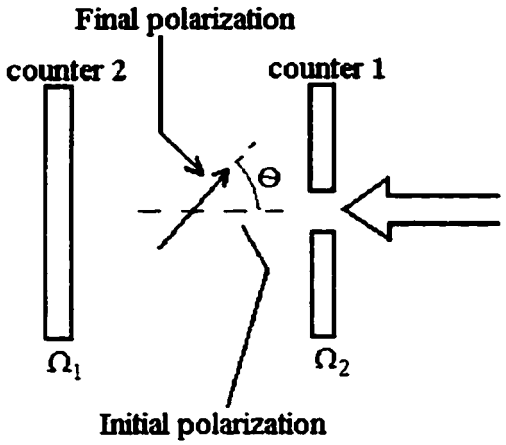

Figure 21: Positron counters used to reconstruct $G_z(t)$.

where N^0 is a common normalization, $\epsilon_\pm$ are the efficiencies of the positron detectors in the z and $-z$ directions, $B_\pm$ are the backgrounds (as determined from the $t < 0$ bins), $A_\pm$ are the "intrinsic" asymmetries of the positron detectors (the count rate is proportional to $(1 \pm A_\pm)$ when the muons are fully polarized along (opposite) the detector axis of symmetry), and $\tau = 2.2$ μsec is the muon lifetime.

The two spectra are combined to form the experimental asymmetry:

$$a(t) = \frac{(N_+(t) - B_+) - (N_-(t) - B_-)}{(N_+(t) - B_+) + (N_-(t) - B_-)}, \tag{24}$$

or:

$$a(t) = \frac{(1-\alpha) + (1+\alpha\beta)A_+G_z(t)}{(1+\alpha) + (1-\alpha\beta)A_+G_z(t)}, \tag{25}$$

where $\alpha \equiv \frac{\epsilon_-}{\epsilon_+}$ and $\beta \equiv \frac{A_-}{A_+}$. The factor $\frac{1-\alpha}{1+\alpha}$ is the "baseline" asymmetry for totally unpolarized muons. One convenient feature of this construction is that the muon lifetime does not appear in the experimental asymmetry.

In practice, one displays the corrected asymmetry, given by:

$$A_+ G_z(t) = \frac{(\alpha - 1) + (\alpha + 1)a(t)}{(\alpha\beta + 1) + (\alpha\beta - 1)a(t)}, \tag{26}$$

The "raw" spectrum from one counter and the corrected asymmetry for TF-μSR data are compared in Fig. 22. As shown, the corrected asymmetry does not depend on the muon lifetime.

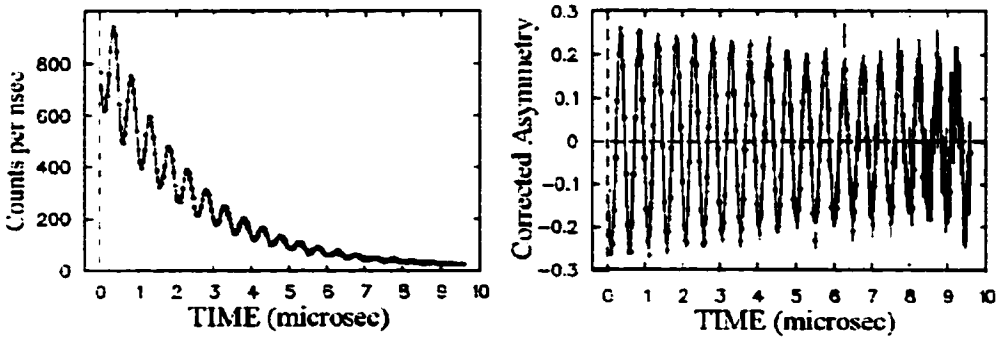

Figure 22: (a) Raw spectrum from one counter. (b) Corrected asymmetry.

The parameters α and β are determined from fits to the data. α is found the easiest way from TF spectra of the opposite counters along the z direction, while β must be determined by simultaneous fits to

the TF "raw" spectra $N_{\pm}$. It is usually assumed that $\beta = 1$, while alpha is allowed to vary. It is not uncommon to assume a value for α by identifying the "baseline" from the ZF spectrum containing the most relaxing data.

3.6 Sample and particularities of the measurement

We measured the sample under zero and longitudinal magnetic field up to 2.7 kG at the M20 channel of TRIUMF using the LAMPF spectrometer. The forward counter consists of two long semi-cylindrical pieces, with the axis along the direction of the muon beam. Because of the difficulty in aligning the counter with the beam, a small fraction of the total signal shows precession with a frequency $\omega = \gamma_{\mu} B$. The longitudinal field measurements were continued up to a field of 6 kG at the M15 channel of TRIUMF, with the Belle spectrometer set up for a conventional LF experiment. With the same spectrometer, we also performed TF measurements under magnetic fields up to 1 T. For all the mentioned measurements, we used surface muons with a 29.8 MeV/c momentum and a single crystal specimen of $8 \times 8 \times 2$ mm in di-

mensions. The largest surface perpendicular to the cubic crystal axis, which is parallel to the muon beam direction.

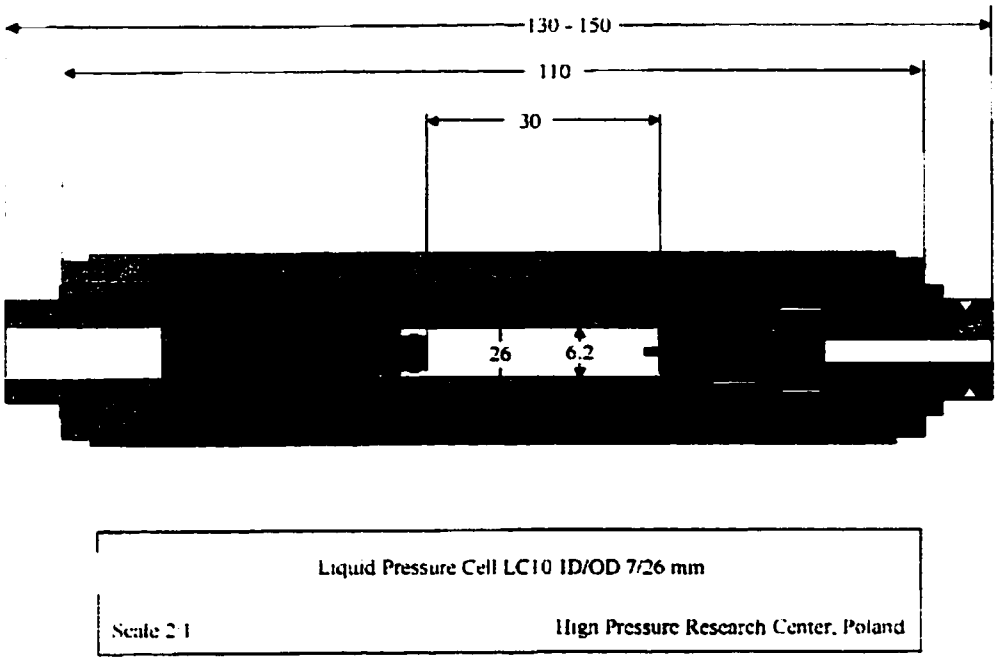

Figure 23: The pressure cell used for measurements under 8.3 kbar.

We also performed measurements under an applied pressure of 8.3 kbar at the M9B channel of TRIUMF, which specializes in high momentum muon beams. To apply the pressure, we used a piston-cylinder pressure cell, shown in Fig. 23, with an outer diameter of 24 mm and an inner diameter of 6.2 mm. The cell was made of the copper-beryllium alloy 25 with a density of 8.35 g/cm^3, and with a composition of 1.9 % Be, 0.2 % Co, 0.1 % Fe, 0.05 % Ni, 0.003 % Cr and the rest copper. The sample is immersed in a pressure transmitting medium, Daphne

oil, which is compressed by a piston using a common hydraulic press. The piston is expected to travel along a distance of 17 mm when the pressure varies from ambient pressure to 13 kbar. The Daphne oil freezes at a temperature between 100 K and 130 K, depending on the pressure. To ensure homogeneity of the pressure, the pressure cell was cooled at a slow rate of 2 K/min in this temperature region. During cooling, the pressure decreases with 2-3 kbar, which reduces considerably the pressure range available.

Because of the thickness of the pressure cell walls, the muon must have a high momentum in order to reach the sample. We run the experiment at the highest momentum (approximately 110 MeV/c) allowed by the current power supply of the superconducting magnet. To minimize the loss of momentum in the cryostat walls, we used a horizontal cold finger cryostat with a mylar window at the sample position. The sample, made of square tiles of MnSi of $3.9 \times 3.9 \times 2 - 3$ mm sitting one on top of another, was 16 mm long. We fixed the sample in place by encapsulating it in a thin-wall tube made of Kapton tape. The temperature was recorded as the average indication of two

GaAlAs thermometers placed close to the ends of the pressure cell. The pressure was determined from the resistivity versus temperature and pressure calibration of a semiconductor pressure gauge SPG10 located inside the cell.

4 Fitting Procedure

4.1 The paramagnetic state

In the paramagnetic phase, the time dependence of the muon spin polarization is determined by the dephasing of the muon precession due to the electronic or the nuclear dipolar spin fluctuations and also to the variable nuclear dipolar field at the muon site. Figure 24 shows the temperature dependence of the muon spin polarization under an applied field of 2115 G. As the temperature increases above $T_c = 29.5$ K, the signal relaxes more slowly.

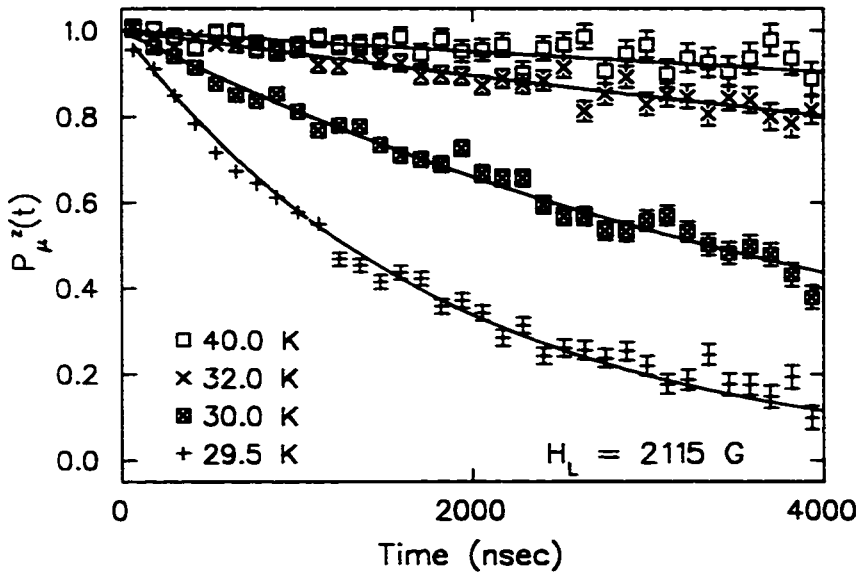

Figure 24: The temperature evolution of the muon spin polarization in the paramagnetic phase, under an applied field of 2115 G. Close to T_c, the signal depolarizes faster.

The longitudinal spin relaxation function is best described as:

$$G_{\mu z}(t) \equiv \frac{< \mathbf{P}_\mu(t) \cdot \mathbf{P}_\mu(0) >}{|\mathbf{P}_\mu(0)|^2}. \tag{27}$$

Since the local field due to electronic spins fluctuates much faster than the nuclear dipolar fields, the ZF longitudinal polarization function can be written as:

$$G_{\mu z}(t) = e^{-\frac{t}{T_1^\mu}} G_{\mu z}^{KT}(t; T_1^{Mn}), \tag{28}$$

where T_1^μ is the relaxation time of the fluctuating electronic spins and T_1^{Mn} is the correlation time of the nuclear dipolar field. The function $G_{\mu z}^{KT}(t; T_1^{Mn})$ is the dynamical Gaussian Kubo-Toyabe function and describes the relaxation due to a Gaussian distribution of local fields fluctuating with the rate $\frac{1}{T_1^{Mn}}$. In the static limit, $T_1^{Mn} \rightarrow \infty$, the Kubo-Toyabe function takes the form:

$$g_{\mu z}^{KT}(t) = G_{\mu z}^{KT}(t; \infty) = \frac{1}{3} + \frac{2}{3}(1 - \Delta^2 t^2) e^{-\frac{\Delta^2 t^2}{2}}. \tag{29}$$

$\frac{\Delta}{\gamma_\mu}$ is the root mean square value of the Gaussian distribution of static nuclear dipolar fields: $\frac{\Delta^2}{\gamma_\mu^2} =< B_x^2 >=< B_y^2 >=< B_z^2 >$. Since the local field from the Mn moments is small, $\frac{\Delta}{\gamma_\mu} \approx 4$ G, magnetic fields

greater than 50 G suppress the nuclear dipolar relaxation making $G_{\mu z}^{KT}(t; T_1^{Mn}) \approx 1$, this way being possible to observe T_1^{μ} independently.

Level crossing resonance (LCR) with nuclear quadrupole oscillation was found in MnSi around $B_{\mathrm{L}} = 100$ G [24]. We carefully avoided this B_{L} and we did not find any signature of the LCR effect in the present study.

4.2 The ordered phase

Under each magnetic field, two precession signals could be identified. Figure 25 shows the muon spin polarization as a function of time and temperature for an applied magnetic field of 2115 G. As the temperature is increased, the amplitude of the oscillating signal decreases considerably.

Previous ZF-μSR studies on MnSi [18] also found two precession frequencies, indicating two muon sites with different magnitudes of internal fields. However, it is difficult to decompose P_{μ}^{z} observed above T_{c} into a sum of two exponential functions having different decay rates. Thus, the results in references [17] and [18] were obtained by using a

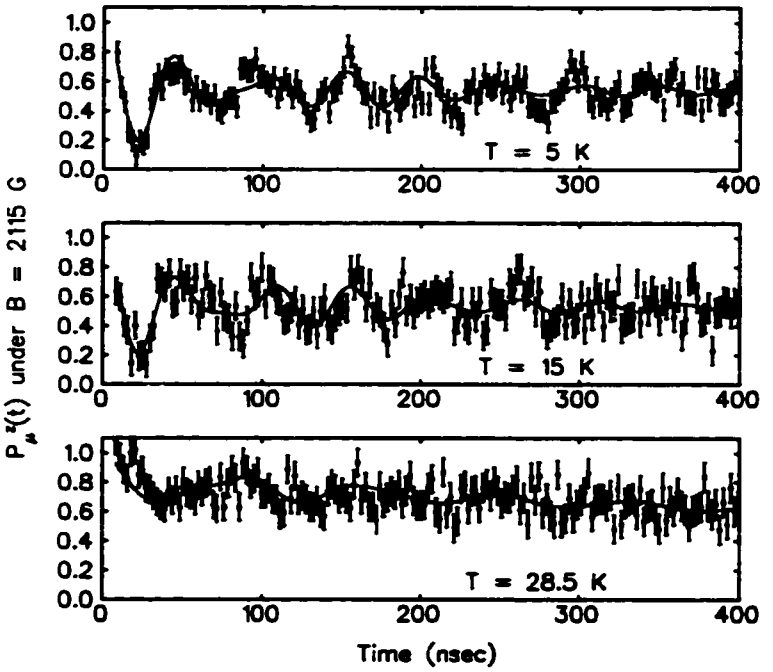

Figure 25: The temperature evolution of the precession signal under an applied field of 2115 G. Two precession frequencies can be seen close to T_c.

single exponential relaxation function for the electron spin contributions. We followed this approach in the analysis of the present data, which allows direct comparison of the T_1 results with the previous measurements.

For the ordered phase data, the muon polarization function was expressed as:

$$P_z^\mu(t) = \sum_{i=1,2} (p_i(\frac{1}{3}e^{-\frac{t}{T_1^{(i)}}} + \frac{2}{3}e^{-\frac{t}{T_2^{(i)}}} cos(\omega_{(i)}t))), \qquad (30)$$

where $T_2^{(i)}$, $i = 1,2$, are the transverse relaxation times and $\omega_{(i)} = \gamma_\mu B_{loc}^{(i)}$ are the precession frequencies around the local magnetic fields

($\gamma_\mu = 2\pi \times 13.55$ kHz/G). p_1 and p_2 are the relative populations of the two inequivalent muon sites, $p_1 + p_2 = 1$.

The transverse relaxation is due to inhomogeneities in the magnitude of the local magnetic field and also to fluctuations of the local field. The factors $\frac{1}{3}$ and $\frac{2}{3}$ from the above expressions are expected to change under an applied magnetic field or for anisotropic single crystals [23]. The nuclear dipolar relaxation can be neglected compared to the effect of the spontaneous magnetic field.

5 Analysis of the longitudinal field data

5.1 Preliminary results

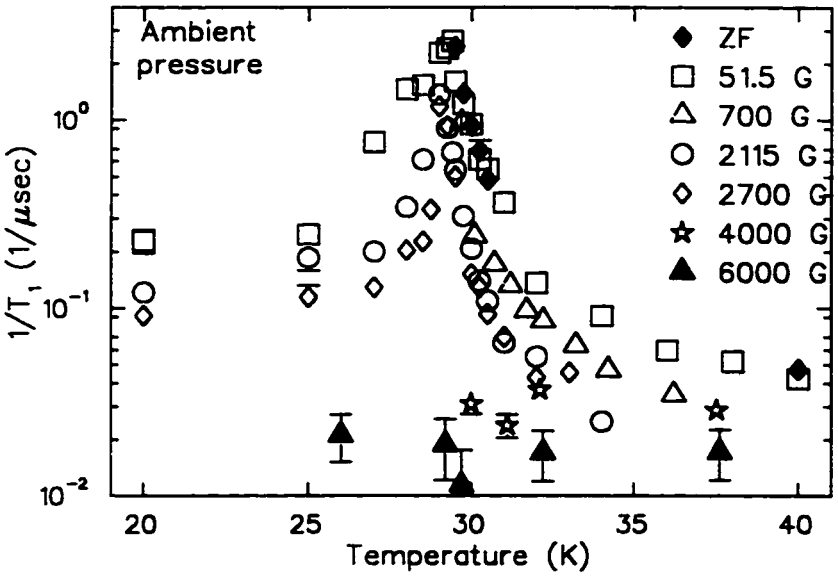

Figure 26: Temperature dependence of the relaxation rate under zero field and applied magnetic fields of 51.5 G, 2115 G, 2700 G, 4000 G and 6000 G. Data under 700 G taken by Dr. Hayano's group is plot for comparison.

In Fig. 26 we present the relaxation rate $\lambda = \frac{1}{T_1}$ as a function of the temperature and of the magnetic field applied. The histogram binning was chosen to average out the precession of the muon spin around the local magnetic field in the ordered phase. This precession signal looses amplitude on a time interval of approximately 500 nsec, much smaller than the 8000 nsec length of the time histogram. Therefore the data in both the paramagnetic and the ordered state could be fitted with

a simple exponential function. For the analysis of the paramagnetic state data, the asymmetry was kept constant, while for the ordered state data it was allowed to vary down to .33 %, when the sample is completely ordered magnetically. This procedure was used in order to get a consistent measurement of the relaxation time over the entire temperature range. More detailed features of the relaxation rate in the ordered phase will be presented later.

As seen in the figure, under magnetic fields up to 2700 G the muon spins still show a pronounced relaxation in the temperature region of the helical transition. A magnetic field of 4000 G or above completely suppresses the critical fluctuations.

5.2 Analysis of results in the frame of the SCR theory

Generally, the nuclear/muon spin-lattice relaxation rate due to electronic spin fluctuations is given by [25]:

$$\frac{1}{T_1} = \frac{\hbar\gamma_\mu^2 T}{N_0} \sum_q \frac{|A_q|^2 \mathrm{Im}\chi^{+-}(q,\omega)}{\omega}, \tag{31}$$

where the z direction is taken along the quantization axis of the muon spins, γ_μ is the muon gyromagnetic ratio, A_q is the Fourier q-component of the hyperfine coupling constant and ω is the energy of the spin excitation, which for practical purposes can be considered $\omega \to 0$. $\chi^{+-}(q,\omega)$ represents the dynamical susceptibility and the imaginary part of $\chi^{+-}(q,\omega)$ gives the intensity of the excitation with the wave-vector transfer q and the energy ω.

5.2.1 Paramagnetic phase

According to SCR, the dynamical magnetic susceptibility in the paramagnetic phase, expressed in units of $(2\mu_B)^2$, is given as:

$$\chi(q,\omega) = \frac{\pi T_0}{\alpha T_A} \frac{1}{2\pi T_0(y+x^2) - \mathrm{i}\omega}, \tag{32}$$

where $y = \frac{1}{2\alpha T_A \chi(0)}$ is the reduced inverse susceptibility, $x = \frac{q}{q_B}$ is the reduced wave-vector, with $q_B = (\frac{6\pi^2}{v_0})^{\frac{1}{3}}$ the effective zone boundary vector and v_0 the volume per magnetic atom, and α is the reduced interaction constant ($\alpha = 1$ at the magnetic instability). T_0 and T_A characterize the energy width of the dynamical spin fluctuation spectrum and the width of the distribution of static susceptibility in the

q-space, respectively.

Neglecting the q dependence of A_q one obtains for the relaxation time of muons the formula mentioned previously:

$$\frac{1}{T_1} = \frac{\hbar\gamma_\mu^2 A_{hf}^2}{2\pi T_A}\frac{1}{\overline{T_1}}, \quad \text{with} \quad \frac{1}{\overline{T_1}} = \frac{3t}{2y}, \tag{33}$$

where $\overline{T_1}$ is the reduced relaxation time and $t = \frac{T}{T_0}$ is the reduced temperature.

If the static susceptibility obeys a Curie-Weiss law, $\chi = \frac{C}{T-T_c}$, the slope of the T_1 versus $\frac{1}{T}$ plot is proportional with the critical temperature. This behavior is expected for the case of itinerant systems at higher temperatures above T_c. The relaxation time of muons T_1 is shown in Fig. 27 as a function of the inverse temperature for magnetic fields of 51.5 G, 2115 G and 2700 G. For temperatures higher then T_c, the T_1 versus $\frac{1}{T}$ plot is linear under each applied magnetic field, but the slope of the plot increases with the field up to magnetic fields of 2115 G. The data taken under 2700 G is superimposed on the data taken under 2100 G. The data taken previously under 700 G by Dr. Hayano [17] is consistent with our experimental results.

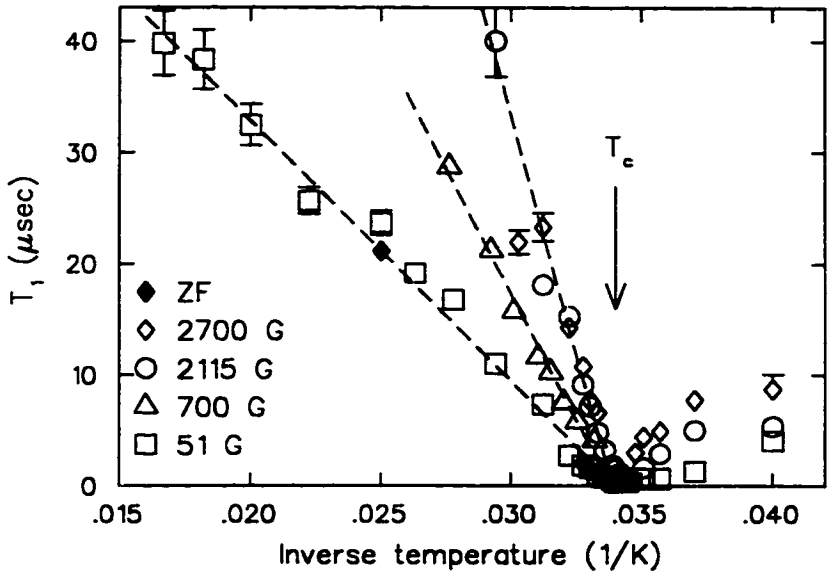

Figure 27: Magnetic field dependence of the relaxation time versus inverse temperature plot; the data shows a good linear dependence of T_1 on $\frac{1}{T}$ at higher temperature under each magnetic field.

Close to the critical temperature, the spin fluctuation modes with small wave-vector and low energy become predominant in itinerant magnetic systems and the uniform susceptibility is expected to deviate from the Curie-Weiss law, $\frac{1}{\chi} \propto (\frac{T}{T_C} - 1)^2$, which results in $T_1 \propto \frac{1}{T}(\frac{T}{T_C} - 1)^2$ [1]. There is also an intermediate region between the high temperature region and the region around T_c where $\frac{1}{\chi} \propto ((\frac{T}{T_c})^{4/3} - 1)$, which is a weakly super-linear dependence of $\frac{1}{\chi}$ on temperature [1].

Improved experimental conditions allowed us to define the sample temperature with much better accuracy ($\pm$ 0.02 K) and to acquire more data, especially in the region around T_c. Fig. 28 shows the plot

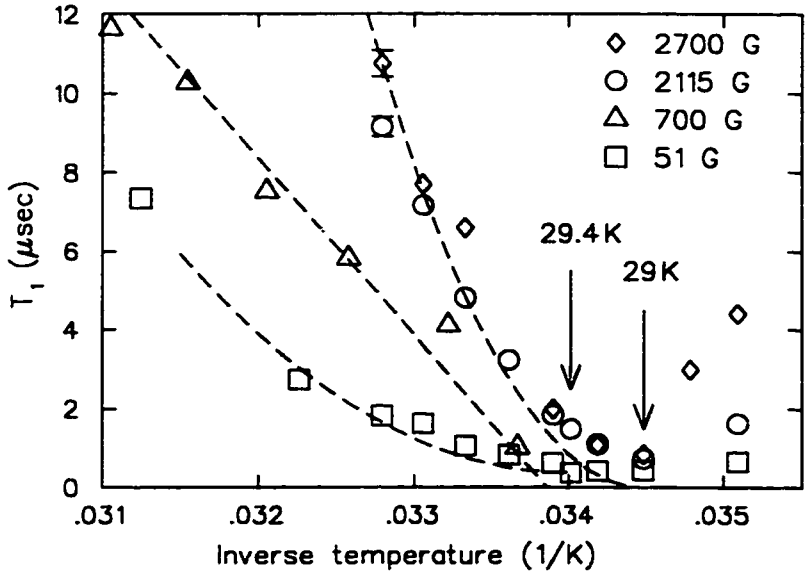

Figure 28: The relaxation time versus inverse temperature plot around T_c, together with the theoretical fit. The data shows departure of the T_1 versus $\frac{1}{T}$ dependence from the linear behavior characteristic for higher temperatures.

of T_1 versus $\frac{1}{T}$ around the transition temperature, together with a fit to the $(\frac{T}{T_c} - 1)^2$ dependence. The values of the critical temperatures, as determined from the peak of the relaxation rate λ versus temperature plot, are 29.4 K and 29 K under 51.5 G and 2115 G, respectively. A slight offset has been added to fit the data under 51.5 G. The data confirms the curving of the T_1 versus $\frac{1}{T}$ plot predicted by the theory. The best fit was obtained for the 2115 G and 2700 G data in the temperature range from 29.5 K ($\frac{1}{T}$ = 0.0339 K^{-1}) to 30.5 K ($\frac{1}{T}$ = 0.0328 K^{-1}). The data taken previously under 700 G by Dr. Hayano is also shown.

5.2.2 Ordered phase

In the ordered phase, the zero field spin lattice relaxation time is given by [1]:

$$\frac{T_{10}}{T_1} = \frac{w_0(\frac{v_0 a_F}{8\pi^3})^2}{\pi\alpha A^2\zeta^2}, \tag{34}$$

where T_{10} is the spin lattice relaxation time in normal metals and it is given by the usual Korringa expression:

$$\frac{1}{T_{10}} = \frac{\pi\gamma_\mu^2 A_{hf}^2}{N_0^2}[\rho(\epsilon_F)]^2 T. \tag{35}$$

A was defined in Eq. 20 for the expansion of the dynamical susceptibility around T_c, v_0 is the atomic volume, a_F is the area of the d-electron Fermi surface, $w_0 = \frac{v_0 N_0}{4\pi^2\rho(\epsilon_F)}$ and $\zeta = \frac{2M}{N_0}$ is twice the magnetic moment per atom.

In an applied magnetic field, the spin lattice relaxation changes according to:

$$\frac{1}{T_1} = (\gamma_\mu A_{hf})^2(\frac{v_0 C}{4\pi^2 A})T\frac{\frac{\zeta}{h}}{1+\mathcal{A}\frac{\zeta^3}{h}}, \tag{36}$$

where C is defined in Eq. 20 in connection to A, $\mathcal{A} = \alpha\overline{A}(\frac{v_0 a_F}{8\pi^3})^{-2}$ and $\overline{A} = \frac{AN_0}{\rho(\epsilon_F)}$ [26].

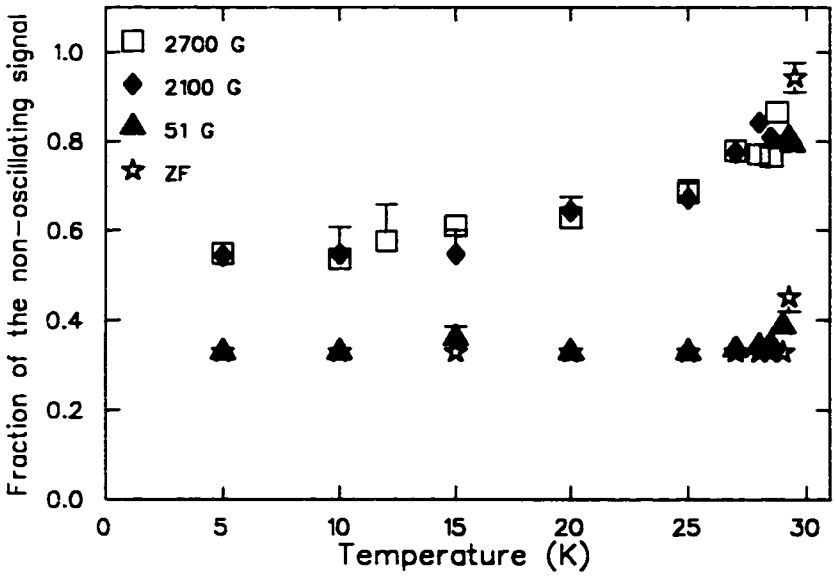

Figure 29: The temperature evolution of the proportion of the non-oscillating signal for various fields. The fraction of the ordered phase decreases as the systems undergoes the transition to the paramagnetic phase.

Muon spin precession was seen up to 29.5 K, 29.4 K, 28.5 K and 28.75 K for zero field, 51 G, 2115 G and 2700 G, respectively. To obtain good fits, we followed the procedure indicated by R. Kadono and his collaborators [18]. We assumed that, as expected in the fast fluctuation limit, the T_1 and T_2 relaxations are proportional to the square of the local magnetic field at the muon site, $T_{1,2}^{(i)} = \theta_{1,2}\omega_{(i)}^2$, $i = 1, 2$, with $\theta_{1,2}$ an effective correlation time common to the two sites.

The factors $\frac{1}{3}$ and $\frac{2}{3}$ from Eq. 30, section **4.2** remained constant up to 29 K under zero field and 51 G, and changed completely under high applied fields. The proportion of the ordered phase decreased as the

system passed through the helical transition from the ordered phase, which results in an increase of the fraction of the non-oscillating signal, as shown in Fig. 29. The transition is not as sharp under high applied magnetic fields as in the case of the lower applied fields.

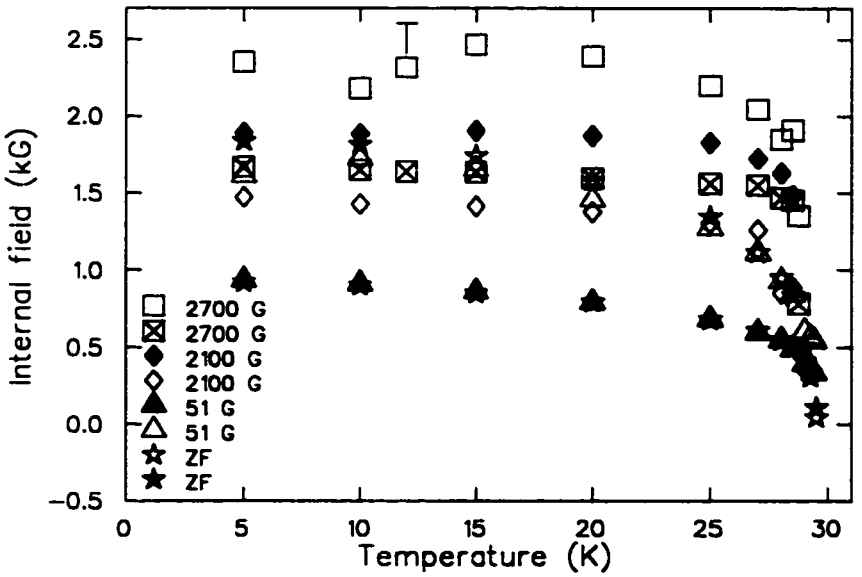

Figure 30: The temperature dependence of the local magnetic field as a function of the magnetic field applied. The magnitude of the local field decreases sharply at the transition temperature.

The magnitude of the local field at the two muon sites was calculated from the precession frequency according to: $\omega = \gamma_\mu B$, with $\gamma_\mu = 2\pi \times 13.54$ MHz/kG. Figure 30 shows the temperature and applied magnetic field dependence of the local field. The very high values of the internal field become more difficult to determine accurately, due to the time resolution of the experiment.

The T_1 relaxation rate corresponding to the two muon sites is shown in Fig. 31. The two relaxation rates show individually the same divergent behavior as indicated previously in Fig. 26.

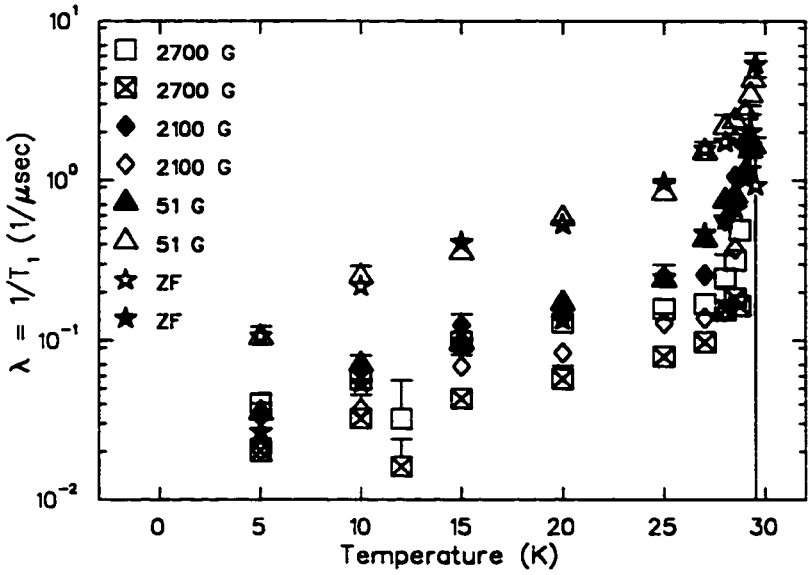

Figure 31: The temperature dependence of the longitudinal relaxation rate, $\frac{1}{T_1}$, as a function of the magnetic field applied. The relaxation rate shows a very pronounced divergent behavior around T_c under each applied magnetic field.

We compared our data with the predictions of the SCR theory for a ferromagnet. Under zero applied magnetic field, $\frac{1}{T_1} \propto \frac{T}{M^2}$, which results in $\frac{M^2}{T_1} \propto T$. Under an applied magnetic field the linear temperature dependence is multiplied by a factor of the form $\frac{M^3}{B+aM^3}$. Because MnSi is a helimagnet with a long period, we apply the above formula, using ω instead of the magnetization. $\frac{\omega^2}{T_1}$ is plot as a function of the temperature in Fig. 32. The plot shows linear behavior up to temper-

atures of 27 K. The data is not precise enough to reveal a departure from the linearity under higher magnetic fields.

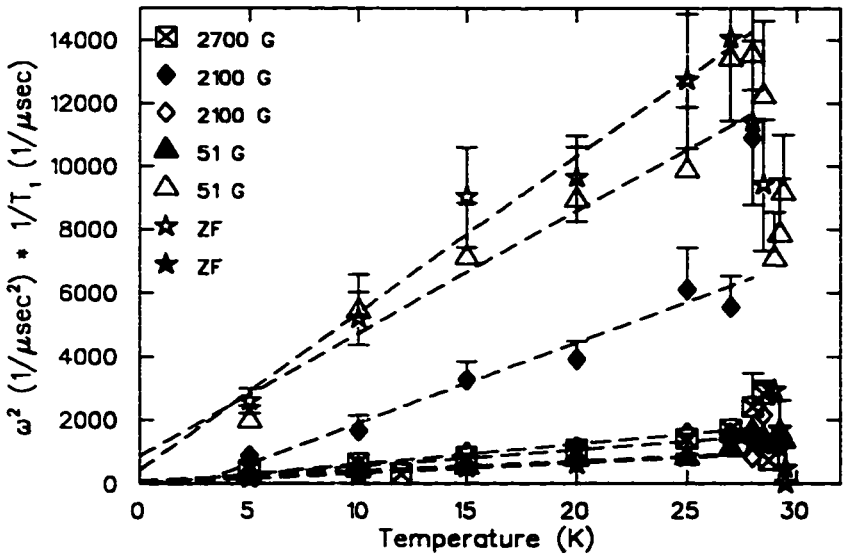

Figure 32: Temperature dependence of the square of the precession frequency multiplied with the relaxation rate. As expected for weak ferromagnetic systems, the plot is linear in temperature up to temperatures close to T_c (approximately 27 K).

Previous experiments by Prof. R. Kadono show up to 20 K the same linear temperature dependence of $\frac{\omega^2}{T_1}$ determined under zero applied field. To justify the departure from linearity above 20 K, it was suggested that the helical structure with a long period might show a behavior closer to antiferromagnetism in the critical region. In the case of a weak antiferromagnet one expects $\frac{M}{T_1} \propto T$ [1]. In Fig. 33 a plot of $\frac{M}{T_1}$ as a function of temperature is shown for the temperature range from 25 to 29.5 K.

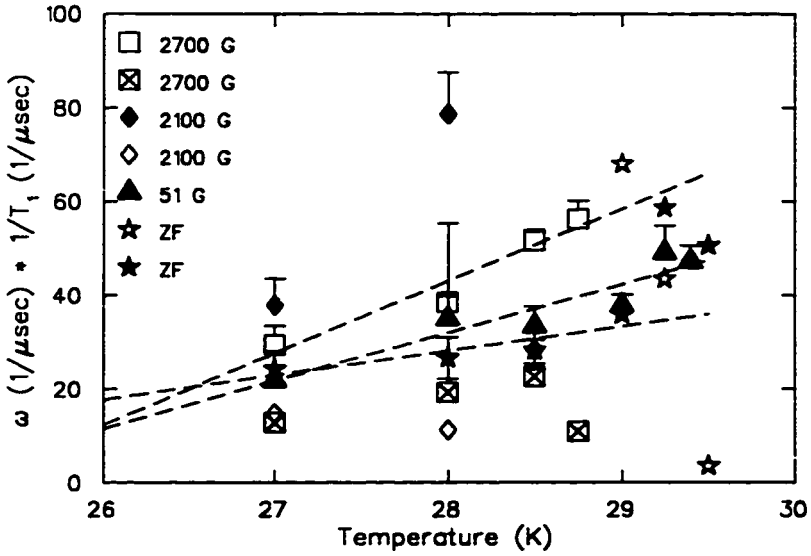

Figure 33: Temperature dependence of the precession frequency multiplied with the relaxation rate. The plot of $\frac{\omega}{T_1}$ is expected to be linear in temperature for helimagnets with a long period.

The data taken under 2700 G, shown with open squares, the data taken under 51 G, shown with filled triangles, and the zero field data up to 29 K, shown with filled stars, are consistent with the expected behavior. Also, the data under 2115 G shown with open rhombic symbols and the data under 2700 G shown with crossed square symbols seem consistent with this trend, but the data is too scattered to fit. The departure from linearity could be attributed to the high tradeoff of fitting parameters close to T_c.

In conclusion, most of the properties of the MnSi system could be explained in the frame of the SCR theory. The linearity of the T_1 versus

$\frac{1}{T}$ plot at temperatures above T_c and the departure from linearity at temperatures close to T_c were shown in a very convincing way. Also, the analysis of the ordered phase data is confirming previous expectations for helimagnetic systems with a long period, such as MnSi.

What it is difficult to explain in the frame of the SCR theory is the field dependence of the slope of the T_1 versus $\frac{1}{T}$ plot at high temperatures above T_c. In what follows we show how the experimental data disagrees with the predictions of the SCR theory and we propose a model to account for the differences.

5.3 Theoretical calculations

Detailed calculations allow us to investigate the validity of the SCR theory on a wider temperature range, including the region around T_c. The SCR method consists in applying quantum statistical theory to the itinerant magnetic system, starting with the microscopic Hamiltonian. In earlier stages of investigation, the zero-point spin fluctuations were assumed to be temperature independent. It was later proven by neutron inelastic scattering experiments on MnSi [27] that their tem-

perature dependence is significant. The most recent version of the theory of spin fluctuations around magnetic instabilities [28] was used, which takes in account this effect.

According to the theory, the parameters needed for a complete description of the system are any four of the following: T_c, T_0, T_A, p, and F_Q (or y_1). p is the value of the ordered moment per atom at $T = 0$, expressed in units of μ_B. F_Q represents the renormalized coupling constant between the spin fluctuation modes with the wave vector around Q ($Q = 0$ for ferromagnets) and is related to the slope of the Arrot plot, the plot of M^2 versus $\frac{H}{M}$:

$$2\mu_B \frac{H}{M} = F_Q[M(T,H)^2 - M(T,0)^2], \tag{37}$$

where M is the magnetization per atom expressed in units of $2\mu_B$. y_1 is the reduced renormalized coupling constant and it is related to F_Q through the relation:

$$F_Q = \frac{2}{3}\frac{T_A^2}{T_0} y_1. \tag{38}$$

There is another relation connecting these parameters, which is characteristic for itinerant ferromagnets:

$$T_c = .1052 p^{\frac{2}{3}} T_A^{\frac{3}{4}} T_0^{\frac{1}{4}}, \tag{39}$$

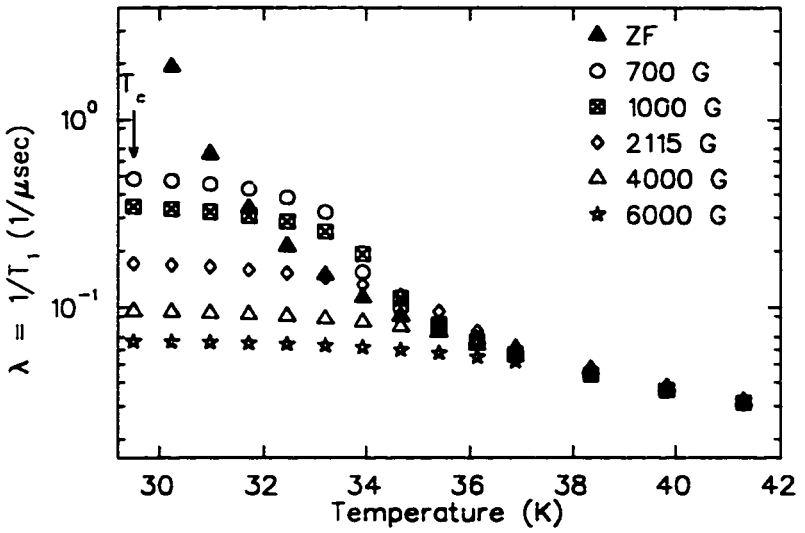

Figure 34: Calculated magnetic field dependence of the muon spin relaxation rate $\lambda = \frac{1}{T_1}$ versus temperature plot in the paramagnetic phase. A magnetic field as small as 700 G suppresses the critical relaxation.

The reduced magnetic susceptibility was defined previously as $y = \frac{1}{2\alpha T_A \chi(0)}$, α being the reduced interaction constant ($\alpha = 1$ at the magnetic instability). For a 3D ferromagnet with itinerant electrons, y in the paramagnetic state takes the following form as a function of the temperature and of T_c, T_0, and y_1 [28]:

$$y = y_1[Y_{31}(y, t; x_c) - Y_{31}(0, t_c; x_c)],$$

$$Y_{31}(y, t; x_c) = 3 \int_0^{x_c} dx x^3 [ln(u) - \frac{1}{2u} - \psi(u)], \tag{40}$$

with $u = \frac{x(y+x^2)}{t}$, $t = \frac{T}{T_0}$, $t_c = \frac{T_c}{T_0}$, and $x_c = \frac{q}{q_B}$. Under an applied magnetic field, the expression becomes more complicated. To determine the magnetic susceptibility, one must solve the magnetic equation of state:

$$y_\perp = -\frac{1}{5} t_A y_1 M_0^2 + t_A y_1 m_T^2 + \frac{1}{20} \frac{b^2 y_1}{t_A} \frac{1}{y_\perp^2}, \tag{41}$$

where M_0 is the value of the spontaneous magnetization per atom at T = 0 K in units of $2\mu_B$, and m_T is the amplitude of the thermal spin fluctuation. m_T can be calculated from:

$$m_T^2 = \Sigma \frac{1+2\delta_{\alpha||}}{5} (m_\alpha^2)_{th}, \quad \alpha = \perp, ||.$$

$$(m_\alpha^2)_{th} = \frac{3}{t_A} \int_0^{x_c} dx x^3 [ln(u_\alpha) - \frac{1}{2u_\alpha} - \psi(u_\alpha)], \tag{42}$$

with $u_\alpha = \frac{x(y_\alpha+x^2)}{t}$. $y_\perp = \frac{b}{2t_A M}$ and $y_{||} = y_\perp + M\frac{\partial y_\perp}{\partial M}$ are the components of the inverse reduced susceptibility perpendicular and parallel to the direction of the magnetization M: $y_\perp = \frac{1}{2T_A \chi_\perp}$ and $y_{||} = \frac{1}{2T_A \chi_{||}}$. $b = \frac{B}{T_0}$ with $B = 2\mu_B H$, H being the external magnetic field.

The parameters values used in calculations were taken from the same reference [28]: T_c = 29.5 K, y_1 = .47, T_A = 2080 K, and T_0 = 231 K. The relaxation time was estimated using the reduced sus-

ceptibilities. Figure 34 shows plot of the calculated relaxation rate, $\lambda = \frac{1}{T_1}$ for different magnetic fields. Even a magnetic field as small as 700 G suppresses the critical fluctuations. This is in contradiction with the experimental results presented previously, which indicated that the critical fluctuations persist up to fields as high as 2700 G.

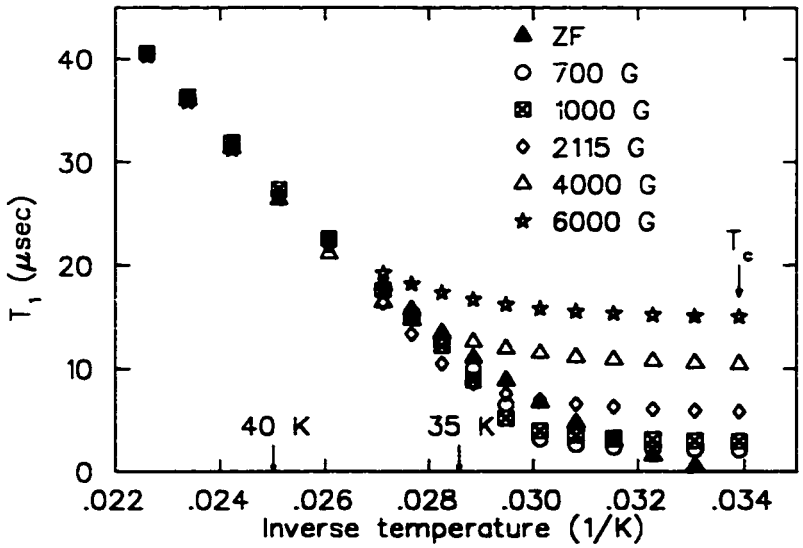

Figure 35: Magnetic field and inverse temperature dependence of the muon spin relaxation time T_1 for MnSi in the paramagnetic phase. Around the critical temperature the spin fluctuations are suppressed by the application of magnetic field, while at higher temperatures the magnetic field dependence of the relaxation time becomes negligible.

At higher temperatures, the plots of the relaxation time T_1 versus inverse temperature for different fields are expected to converge along a single line, as shown in Fig. 35, which again contradicts the experimental data.

5.4 Proposed explanation for the departure from the predictions of the SCR theory

It was for a long time assumed that, because the helical structure has such a long period, the system behaves as a weak ferromagnet for which the application of a small magnetic field suppresses the critical fluctuations. The magnetic field dependence of the relaxation time is rather unexpected.

To explain this behavior we propose a simple model which takes separately into account the contributions to muon spin relaxation from: (a) the $q = 0$ component of spin fluctuations along the direction of the external magnetic field and (b) the spin fluctuations of the remaining helical component in the plane perpendicular to the magnetic field. Accordingly, the muon spin relaxation rate in MnSi can be expressed as $\frac{1}{T_1} = (\frac{1}{T_1})_{\text{parallel}} + (\frac{1}{T_1})_{\text{perp}}$. In view of the dependence of the relaxation time on the Larmor precession frequency of the muon spin around the local field and on the local field fluctuation rate ν, $\frac{1}{T_1} \propto \frac{\omega^2}{\nu}$, one expects the first term to be proportional with the component S_z^2 of electronic spin fluctuations parallel to the magnetic field applied along the z

direction and the second term to be proportional with $S^2_{x,y}$. Here we assume that $S^2_z \propto \frac{B^2_L}{B^2_{max}}$ and $S^2_{x,y} \propto \frac{(B^2_{max}-B^2_L)}{B^2_{max}}$, where B_{max} denotes the value of B_L required to eliminate the helical component of critical spin fluctuations.

In the ordered state at $T = 4.2$ K, the external field $B_L = 6.2$ kG is sufficient to eliminate the helical component, aligning all the spins ferromagnetically, as was shown in Fig. 8. Although it is difficult to have an accurate *a priori* estimate for B_{max} in the paramagnetic state, we expect B_{max} to be of the order of magnitude of 6.2 kG.

According to the calculations, the critical behavior due to ferromagnetic spin fluctuations is suppressed completely above $T = 30$ K for $B_L \geq 700$ G, as shown in Fig. 34. Therefore we assumed that $(\frac{1}{T_1})_{parallel}$ is negligibly small above $T = 30$ K. The observed value of $\frac{1}{T_1}$ reflects only the contribution from helical spin fluctuations, which translates into $\frac{1}{T_1} \propto (B^2_{max} - B^2_L)$.

In Fig. 36, we show the observed relaxation rate $\frac{1}{T_1}$ as a function of B^2_L at 30 K, 31 K, and 32 K. The data taken at 31 K and 32 K is not quite conclusive, but the magnetic field dependence of the data taken

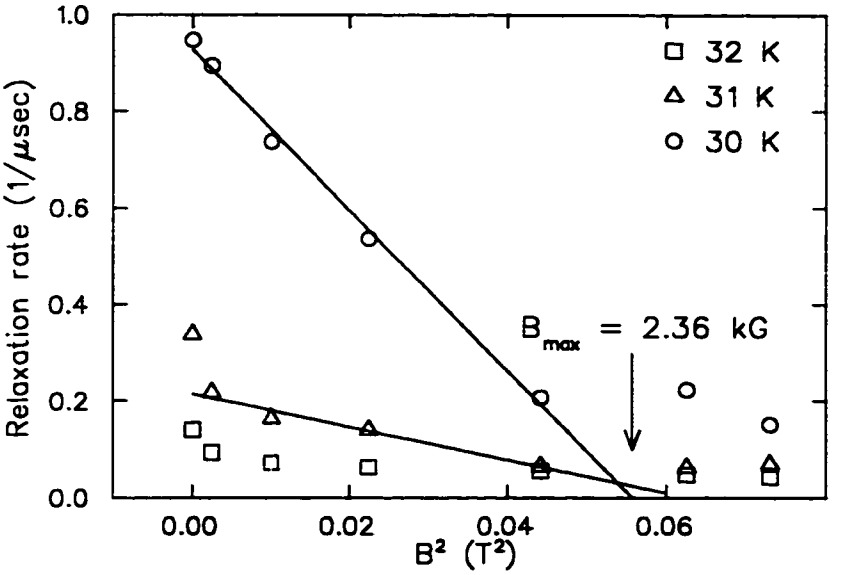

Figure 36: The dependence of the relaxation rate at 30 K, 31 K and 32 K on the square of the magnetic field applied.

at 30 K confirms the above prediction. From the linear fit, we obtained $B_{\max} = 2.36$ kG. The fit for the data at 31 K is also consistent with this value of $B_{\max}$, except for the lowest field point. As can be seen in the phase diagram of MnSi from Fig. 8, the magnetic field of 2 to 3 kG near T_c induces a ferromagnetic state in the system. Therefore, the value of $B_{\max}$ obtained in our experiment is consistent.

This result indicates that even in the paramagnetic state above T_c, the system has a memory of the phase to which it orders with decreasing temperature for a given value of B_L. The application of uniform field B_L suppresses the spin fluctuation of the $q = 0$ component

selectively, while the helical critical fluctuations survive up to $B_{\mathrm{L}} = B_{\mathrm{max}}$.

According to Nakanishi [29] *et al*, in the case of an itinerant electron ferromagnet with no inversion symmetry, the spin-lattice interaction could create a helical spin density wave (HSDW) with a long period. The antisymmetric spin-lattice interaction must be sufficiently small, while the exchange energy favors a ferromagnetic ground state. A finite contribution to the antisymmetric part of the wave-vector dependent dynamical susceptibility is obtained. In MnSi, the ferromagnetic spiral is caused by a Dzyaloshinski-Moriya (DM) interaction which arises because of the non-central arrangement of the Mn magnetic atoms in the unit cell. This interaction makes also the spin spiral right handed, as it was shown by neutrons scattering experiments [30]. Polarized neutron scattering experiments performed on the MnSi system in 1983 [31] have shown that the one-handed spiral has a strong influence on the scattering in all regions of the field-temperature phase diagram.

Polarized neutron scattering experiments along the [0,q,q] crystallographic direction were performed recently on MnSi under a very small

magnetic field of 10 G [32]. The cross section for neutron scattering could contain a term which depends on the initial polarization of the neutron:

$$(\mathbf{Q} \cdot \mathbf{P_i})(\mathbf{Q} \cdot \mathbf{B}), \tag{43}$$

where $\mathbf{B}$ is an axial vector defined as a function of the asymmetric part of the Fourier transform of the spin correlation function, and $\mathbf{Q}$ is the scattering vector. The DM interaction vector in MnSi has a component along the [0,1,1] crystallographic direction inducing spin fluctuations that are centered at positions incommensurate with the chemical lattice. The polarization dependent scattering in the paramagnetic state determined experimentally is an indication of fluctuations with chiral nature. The result was interpreted in terms of the Dzyaloshinski-Moriya (DM) interaction produced by antisymmetric spin interactions persisting at temperatures above the transition due to the noncentrosymmetric crystal structure of MnSi.

In the ordered state the direction of the spin spiral is determined by the crystalline anisotropy and dipolar interactions. The positions

of the maximum and minimum intensity in the paramagnetic state are not located at the incommensurate positions of the magnetic Bragg peaks in the ordered phase. The polarized neutron scattering data indicate that the direction of propagation vector of the spiral in the ordered phase is due to anisotropies that are lost above T_c. Well above T_c the anisotropy disappears and the dipolar interactions become so weak that the spin fluctuations become isotropic.

Most probably, the presence of the incommensurate spin fluctuations affected our data creating the field dependence of the relaxation time described above.

It was shown in a theoretical work of K. Makoshi and T. Moriya [33] that at sufficiently low temperatures a weak helical magnet is expected to have a behavior closer to antiferromagnets. In some helical systems such as MnSi, there is a crossover at higher temperatures from a behavior similar to an antiferromagnet to a behavior of a ferromagnet, but this is not characteristic to the helical spin structure with a long period and small anisotropy.

The authors performed calculations of the uniform and staggered

susceptibilities above the transition temperature of MnSi. It was found that the staggered susceptibility is almost identical to the uniform susceptibility, which obeys a Curie-Weiss law.

In view of the results of neutron scattering experiments, showing the significance of incommensurate spin fluctuations in MnSi, and of theoretical considerations for helical magnets, we tried to investigate the MnSi system close to T_c using the theory for weak antiferromagnets.

Generally, for an antiferromagnet, the relaxation time is given by:

$$\frac{1}{T_1} = \frac{\hbar\gamma_\mu^2 A_{hf}^2}{2\pi T_A}\frac{1}{\overline{T_1}}, \quad \text{with} \quad \frac{1}{\overline{T_1}} = \frac{3\pi t}{4\sqrt{y}}, \tag{44}$$

with y the reduced inverse susceptibility. High above T_c, where the magnetic susceptibility obeys a Curie-Weiss law, the relaxation time T_1 depends on temperature as follows:

$$T_1 \propto \frac{(T - T_N)^{0.5}}{T}. \tag{45}$$

At the antiferromagnetic to paramagnetic crossover, one expects $\frac{1}{T_1} \propto T^{0.25}$ [25]. Following a work on weak itinerant antiferromagnetism of K. Nakayama and T. Moriya [34], I assumed that for finite T_c the staggered susceptibility depends on temperature as $\frac{1}{\chi_Q} \propto (\frac{T}{T_N})^{3/2}$,

therefore $\frac{1}{T_1} \propto \frac{T}{\sqrt{(T^{3/2}-T_c^{3/2})}}$. which reduces to $\frac{1}{T_1} \propto T^{0.25}$ for $T_c \rightarrow 0$. Figure 37 shows a fit of the data to the above temperature dependence. The data taken under 51 G is in agreement with this predictions.

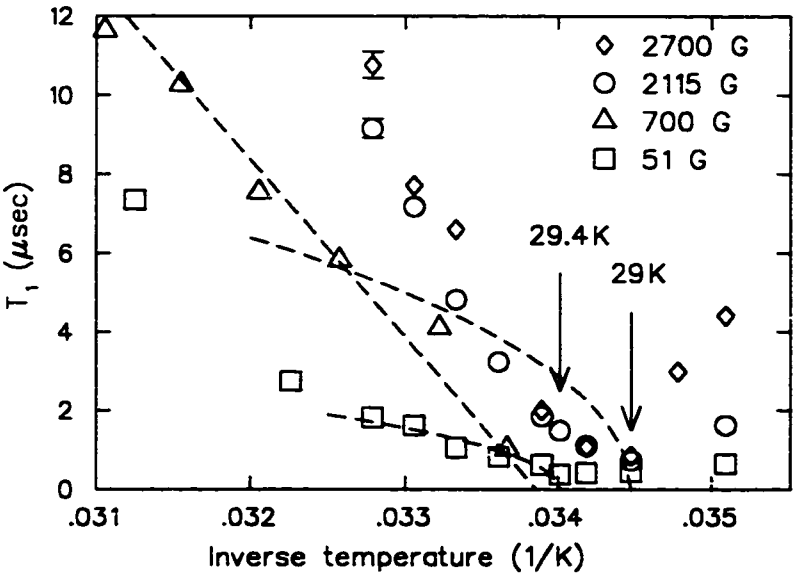

Figure 37: The relaxation time versus inverse temperature plot around T_c, together with a fit to the dependence for a weak antiferromagnet.

μSR can not completely separate the ferromagnetic and the helical spin fluctuations. The data under 51 G could be strongly affected by the incommensurate spin fluctuations, but we consider the data taken above B_{max} (at 2700 G) relevant for the ferromagnetic properties of the system. Both the linearity of the slope of the T_1 versus $\frac{1}{T}$ plot at high temperatures and the curving of the plot around T_c were indicated rather well.

It has also been shown by A. Buzdin and Y. Meurdesoif that in the case of helicoidal structures as that of MnSi, new localized states appear at the helicoidal transition around the crystal defects [35]. The main defects in MnSi are dislocations, but even a point-like local increase in transition temperature can give rise to a localized state. The easy broadening of the transition temperature may be an inherent effect. The single crystal studied shows a rather sharp transition, which takes place on a temperature interval from 29 K to 29.75 K with no applied field. Also, as μSR is a volume probe, the contribution to the relaxation function due to the local defects is expected to be small. Therefore, we conclude that the field dependence of the μSR result on MnSi in the paramagnetic state is an intrinsic property of the system, deeply connected to the helical nature of the magnetic structure.

6 Transverse field measurements

6.1 Transverse Field Experiments and Fitting Procedure

We performed temperature scans of the MnSi sample under transverse magnetic fields of 4 kG, 6 kG, and 1 T. Figure 38 shows the transverse field precession signal at 5 K, 33 K, and 50 K under the applied magnetic field of 1 T. Two precession frequencies can be clearly distinguished at lower temperatures. At higher temperatures, they can be separated from the beating signal.

Under each applied magnetic field, the sample shows two precession frequencies, with the amplitude ratio $p_1 : p_2$, $p_1 + p_2 = 1$. The relaxation function takes the following form:

$$P_\mu^x(t) = p_1 e^{-\frac{t}{T_2^{(1)}}} \cos(\omega_{(1)} t) + p_2 e^{-\frac{t}{T_2^{(2)}}} \cos(\omega_{(2)} t), \qquad (46)$$

where $T_2^{(i)}$ $(i = 1, 2)$ are the transverse relaxations corresponding to the two muon sites and $\omega_{(i)}$ $(i = 1, 2)$ are the precession frequencies around the local field, respectively. The dipolar field width in MnSi

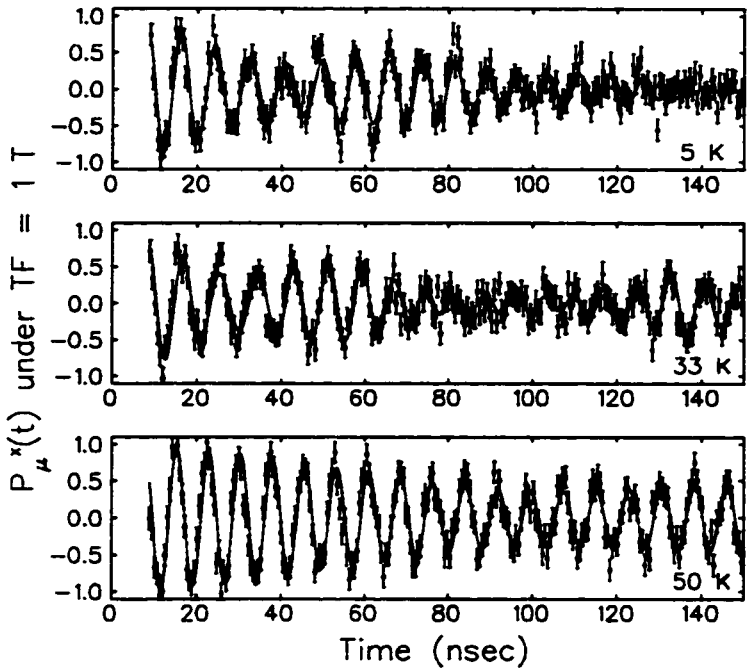

Figure 38: The precession signal under the applied field of 1 T at 5 K, 33 K and 50 K. Two precession frequencies can be distinguished.

is $\Delta = 2\pi(13.54\ \text{MHz/kG}) \times (0.004\ \text{kG}) \approx 0.3\ \mu\text{sec}^{-1}$. The range of our measurements is roughly 1.5 μsec, which corresponds to $t \cdot \Delta \approx .5$ on the plot of the high field transverse relaxation function in Fig. 39. Therefore, we could neglect the contribution to the relaxation function from the fluctuating nuclear dipolar fields in what follows.

The transverse relaxation of muon spins, T_2, is determined by both the static and the dynamic components of the local field. In the limit of fast fluctuating fields, the transverse relaxation rate is given by $G_x(t,\nu) = exp(-\frac{\Delta^2}{\nu}t)$, where $\Delta = \sqrt{< H_z^2 >}$ represents the static field

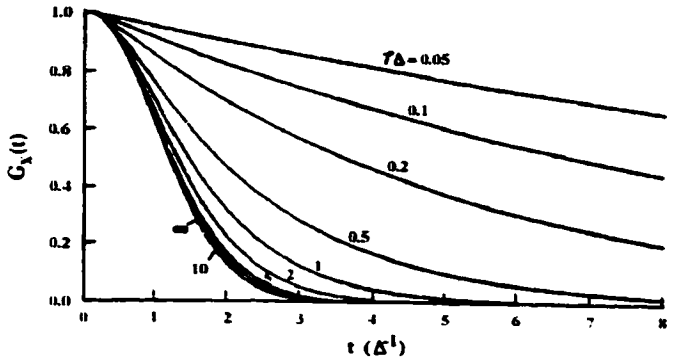

Figure 39: High-field transverse relaxation function plotted for different values of $\tau = \frac{1}{\nu}$, the correlation time of the field fluctuations [36].

width along the applied field direction and ν represents the local field fluctuation rate. To get good fits to the data, we used the procedure followed for the analysis of the longitudinal field data. We assumed that the T_2 relaxations are proportional to the square of the local magnetic field at the muon site, $T_2^{(i)} = \theta\omega_{(i)}^2$ $(i = 1, 2)$, with θ an effective correlation time common to the two sites.

6.2 Experimental Data

Figure 40 shows the temperature dependence of the local field determined by μSR under each applied magnetic field. We interpret the continuous decrease of the magnitude of the local field with decreasing temperature as the transition to the polarized state. The broad range

of the transition is consistent with previous measurements of ultrasonic attenuation.

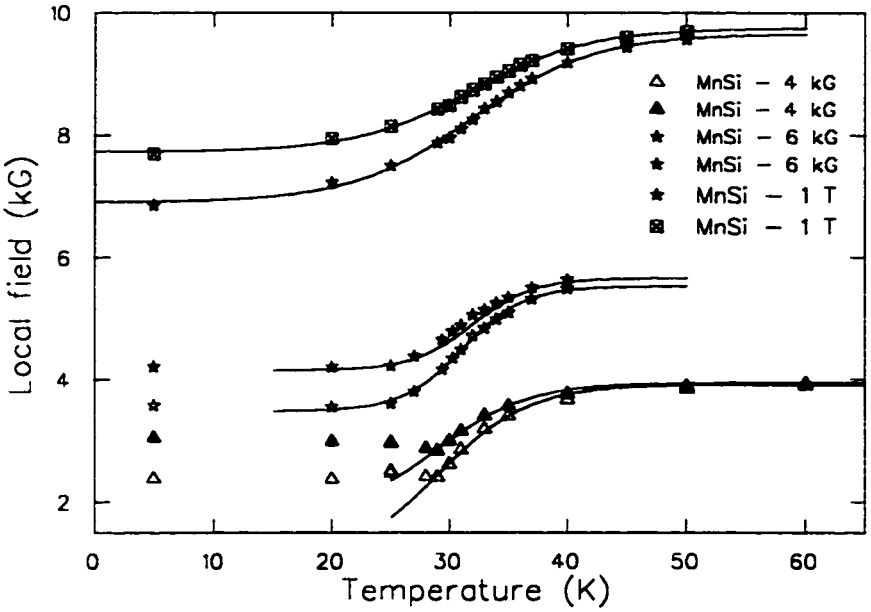

Figure 40: Temperature dependence of the local field under applied transverse fields of 4 kG, 6 kG and 1 T. The value of the local field decreases as the spin system becomes polarized and then stays approximately constant in the helically ordered phase.

Under the applied magnetic field of 4 kG, below the transition to the helical state at 29 K, the magnitude of the local field shows a slight increase. At lower temperatures, the local field is approximately constant. Under 6 kG, the transition temperature to the helical state is 12 K. Both local fields at 5 K show a slight increase in magnitude compared to the local fields at 20 K, similar to the behavior of the system under 4 kG. Under 1 T, the local field decreases smoothly.

No trace of helimagnetism can be detected, as one expects from the field-temperature phase diagram.

6.3 Data Analysis

We explain the temperature dependence of the local field based on a simple model of the local field at the muon site. In calculating the local field, we account for the contributions of the applied magnetic field, the demagnetization field, and the hyperfine field. The magnetic field induction B is measured in gauss and the intensity of the local field H is measured in oersted, as is common for μSR data analysis.

6.3.1 Quantitative description of the local field at the muon site

It is convenient to separate the contributions to the magnetic field by dividing the magnetic material in two regions. Inside a sphere of suitable diameter, called the Lorentz sphere, the sources of magnetic fields are treated individually, while the continuum approximation is applied outside this sphere. The total magnetic field at the μ^+ can be

expressed as follows:

$$B_\mu = B_{ext} - B_{DM} + B_L + B_{hf} + B_{dip}, \tag{47}$$

where B_{ext} is the externally applied field, B_{DM} is the demagnetization field due to the surface magnetization of the finite sample, B_L is the Lorentz field produced by the empty Lorentz sphere inside the magnetized environment, B_{hf} is the contact hyperfine field at the muon site (including the diamagnetic effects), and B_{dip} is the net field from magnetic dipoles inside the Lorentz sphere [37]. Figure 41 shows the macroscopic magnetic field inside the Lorentz sphere.

The demagnetization field and the Lorentz field depend on the magnetization as follows:

$$B_L = \frac{4\pi}{3}M, \quad B_{DM} = -NM, \tag{48}$$

where N is the demagnetization factor. The demagnetization factor for our sample, of dimensions $8 \times 8 \times 2.5$ millimeters, is around 9, if one uses the system of units indicated previously. It was calculated assuming that the sample has uniform magnetization, by integrating over the field due to the surface density of the magnetic charge.

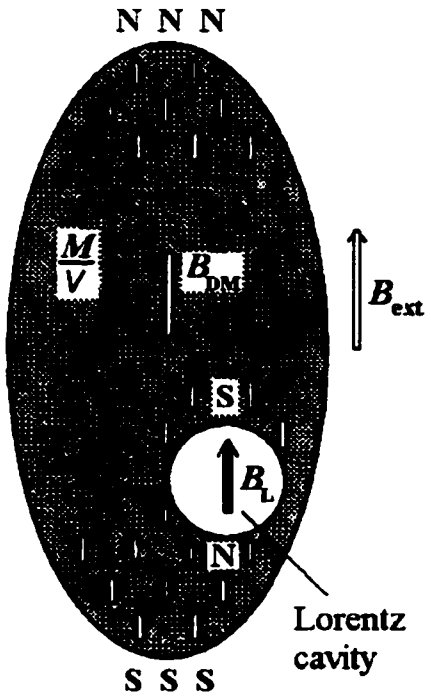

Figure 41: Macroscopic magnetic field inside the Lorentz sphere. In the continuum approximation the magnetic dipoles outside the cavity will produce a field inside the cavity given by $B_{DM} + B_L = -(N - \frac{4\pi}{3})M$, where M is the magnetization of the sample and N is the demagnetization factor [37].

The dipolar field is the summation of all fields b_i from the magnetic moments at positions r_i located inside the Lorentz sphere. For a cubic crystal such as MnSi, the dipolar field is zero.

$$B_{dip} = \sum_{r \subset \Omega^L} b_i(r_\mu - r_i) \approx 0 \tag{49}$$

The contact field or the hyperfine field is determined by the electronic structure around the muon site:

$$B_{hf}(r_\mu) = \frac{8\pi}{3}[n^+(r_\mu) - n^-(r_\mu)], \tag{50}$$

where $n^+(r_\mu)$ is the density of spin-up electrons at the muon site and is $n^-(r_\mu)$ the corresponding spin-down density. Their difference is the net spin density at the muon site. A non-zero spin density may be the result of spontaneous magnetic ordering or can be caused by an external field, via the Pauli spin paramagnetism of the conduction electrons. In the first case, the ordered electronic moments induce, via exchange interactions, a spin polarization of the conduction electrons which produces the contact hyperfine field at the μ^+. The spontaneous hyperfine field is related to the domain magnetization M via the relation $B_{hf} = A_{hf}M$. It is convenient to express the hyperfine coupling constant A_{hf} in units of kOe/μ_B and the magnetization M in units of μ_B/Mn.

In the MnSi system, under applied magnetic fields higher than 1 kG, the helical axis aligns with the direction of the external magnetic field. Therefore the macroscopic magnetization is also parallel to this field. The following equation will then hold:

$$B_{\mu||} = B_{ext} - NM + \frac{4\pi}{3}M + A_{hf}M + B_{dip}, \qquad (51)$$

where $B_{\mu||}$ is the component of the local field parallel to the magnetization.

The contact term produces in MnSi a negative contribution to the total local magnetic field. The hyperfine coupling constants corresponding to the two muon sites were determined from measurements in the ordered state under zero applied field [18] and are A_{hf}^1 = -3.94 kOe/μ_B and A_{hf}^2 = -6.94 kOe/μ_B, respectively. A different value, A_{hf}^1 = -4.8 kOe/μ_B, was obtained from Knight shift measurements in the paramagnetic state under 2.9 kG [17]. This value yields results consistent with our measurements under high applied field, and we use it for the rest of the discussion.

6.3.2 Magnetization results

In the paramagnetic phase $B_{\mu||} = B_\mu$. The sample magnetization can be obtained in the most convenient way by subtracting the values of the magnetic fields at the two muon sites:

$$M = \frac{B_\mu^1 - B_\mu^2}{A_{hf}^1 - A_{hf}^2}. \tag{52}$$

This fortunate procedure eliminates the inaccuracy in determining

the demagnetization and the dipolar contributions to the total local magnetic field, but it is valid only for the paramagnetic state. By μSR, one can determine the total value of the local field, but not θ, the angle made in the helical state by the local field and the applied field ($B_{\mu||} = B_{\mu}cos(\theta)$).

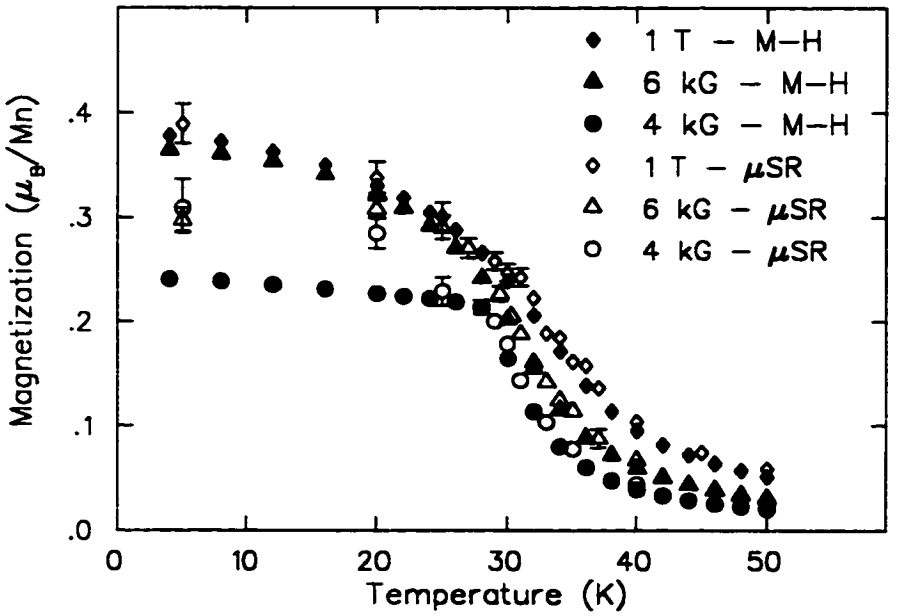

Figure 42: Temperature dependence of the magnetic moment per Mn atom under 4 kG, 6 kG and 10 kG, as determined from both μSR and magnetic susceptibility measurements. The data shows excellent agreement.

We compare the μSR data with magnetization data obtained at Columbia University. Figure 42 presents the results of both measurements, scaled so that the magnetizations at T = 5 K and B = 1 T are comparable. The agreement is excellent, except for the data taken in the helical state, as explained previously. The actual magnetization

result at T = 5 K and B = 1 T is consistent with other measurements, $M_0 = .42\ \mu_B$/Mn.

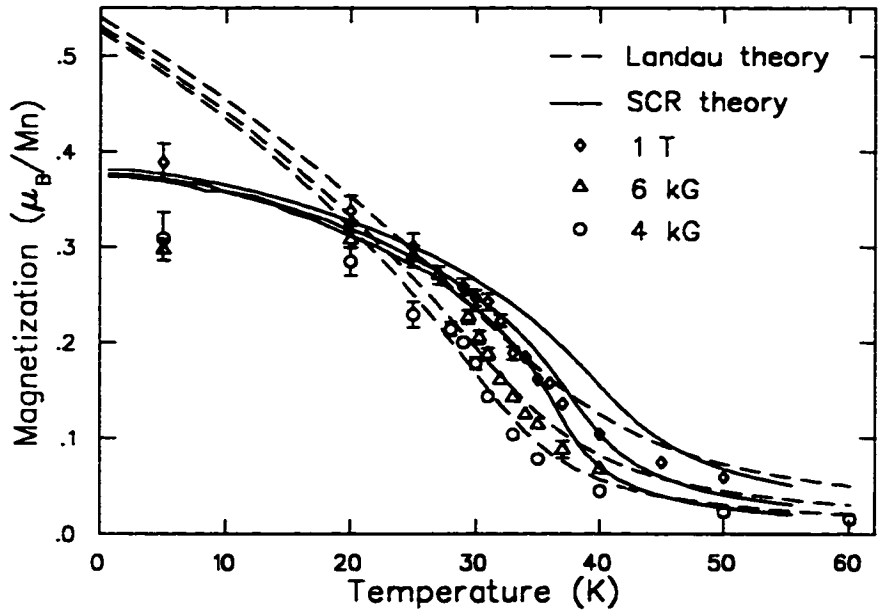

Figure 43: Temperature dependence of the magnetic moment per Mn atom under 4 kG, 6 kG and 1 T. The predictions of the SCR and Landau theories are shown by the solid and the dashed lines, respectively.

To check the validity of the SCR theory, we performed theoretical calculations for 4 kG, 6 kG and 1 T. The same magnetic equation of state holds over the entire field - temperature phase diagram of the itinerant ferromagnetic systems. Therefore, we could follow the procedure outlined for the T_1 calculations. We made use of the same parameters as previously indicated. The resulted magnetization is shown in Fig. 43. The theoretical line reproduces well the shape of the magnetization versus temperature plot, even if the agreement is not prefect.

We also compared the prediction of the SCR theory with the predictions of Landau theory for second order phase transitions. In the frame of the Landau theory, the free energy of the magnetic system is given by:

$$\Phi(p,T,M) = \Phi_0(p,T) + A(p,T)M^2 + B(p)M^4 - MBV, \qquad (53)$$

with $A(p,T) = a(p)(T - T_c)$ and $B(p) > 0$ as the temperature and pressure dependent coefficients, respectively. For $a(p) > 0$, the asymmetrical phase is realized at $T < T_c$, as desired for magnetically ordered systems. The average magnetization is determined from:

$$\overline{M} = \frac{\partial \Phi(p,T,h)}{\partial M}. \qquad (54)$$

Therefore, in a thermal equilibrium state $(\frac{\partial \Phi}{\partial M})_{p,T,h} = 0$, the magnetic equation of state is:

$$2a(T - T_c)M + 4BM^3 = VB. \qquad (55)$$

The magnetization calculated from this magnetic equation of state is shown with dashed lines in Fig. 43. The parameters used for calculations are $\frac{2a}{V} = 0.657$, $\frac{4B}{V} = 72.805$ and $T_c = 29.5$ K. $\frac{2a}{V}$ and $\frac{4B}{V}$ were

determined from a fit to the data under 1 T, with T_c being held constant. We see that the shape of the magnetization versus temperature plot is very different than the one experimentally determined.

In conclusion, the SCR theory gives a much better prediction for the overall temperature dependence of the magnetization as compared to the prediction of the Landau theory.

6.3.3 Discussion of the T_2 measurements

As the temperature decreases, the signal depolarizes faster under all applied fields. For a sample of the given dimensions, the demagnetization field at the edge of the sample is about 30 % less than the demagnetization field in the center of the sample. The higher dephasing rate of the muon spin precession could be produced by the inhomogeneity created by the demagnetization field, and it is not an intrinsic property of the spin system.

In conclusion, the high transverse field measurements do not constitute a good method for determining the relaxation time of fluctuating spins in MnSi. Longitudinal field measurements are more suited for

this purpose.

7 Muon spin relaxation studies of MnSi under applied pressure

Another interesting issue of the SCR theory is the crossover from itinerant ferromagnet to a correlated paramagnet. Since MnSi embodies this crossover in applied pressure, extensive studies have been performed by magnetic susceptibility, resistivity [19], and NMR [22] measurements to explore regions near quantum critical point at p_c = 14.6 kbar.

7.1 Preliminary measurements at PSI

We performed preliminary measurements of a powdered MnSi sample under applied pressure at Paul Scherrer Institut (PSI).

We obtained results for the dynamical muon spin relaxation time around the critical temperature and for the precession frequency of the muon spins at 5 K under applied pressures up to $p = 0.43\ p_c$ (6.3 kbar).

In Figure 44, we present the corrected asymmetry measured under an applied field of 100 G as a function of temperature. Under all

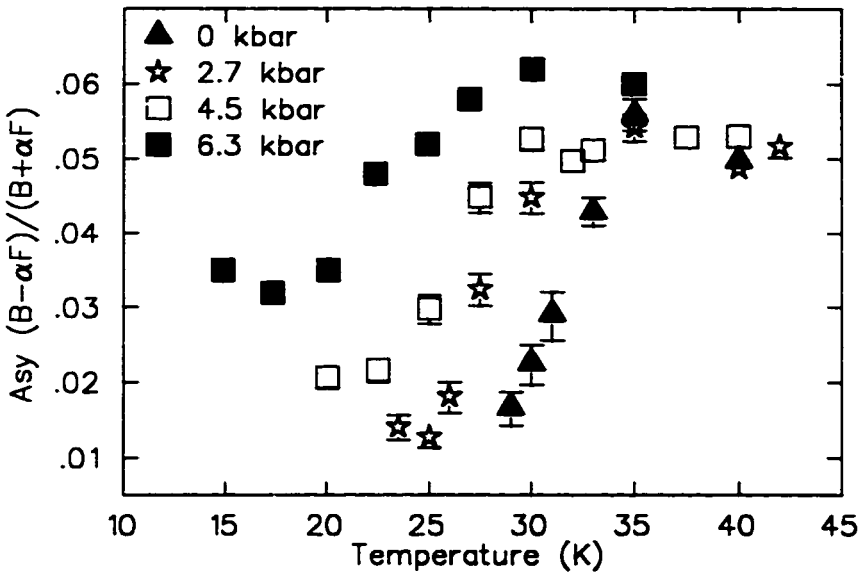

Figure 44: Muon initial asymmetry as a function of temperature under zero and applied pressures of 2.7, 4.5 and 6.3 kbar.

applied pressures, the asymmetry decreases over a broad temperature interval as the sample orders magnetically. It is possible that the application of pressure in our powdered sample created some inhomogeneity, resulting in a broadening of the transition temperature.

Under an applied field of 100 G, the nuclear dipolar contribution to the relaxation function is suppressed. We parametrized the results around T_c after fitting the data with a stretched exponential, $G_z(t) = exp(-(\lambda' t)^{\beta})$, assuming that the relaxation of the muon spin polarization is only due to electron spin dynamics. We defined the relaxation time T_1 as the time needed for the asymmetry to reach half of

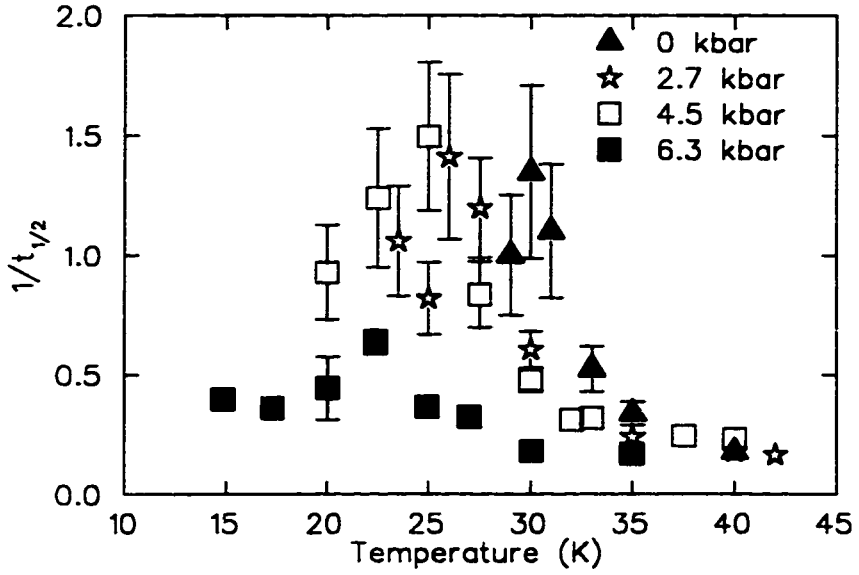

Figure 45: Dynamical relaxation rate of the muon spins as a function of temperature in the MnSi sample under zero and applied pressures of 2.7, 4.5 and 6.3 kbar.

its initial value: $t_{1/2} = \frac{(ln(2))^{1/\beta}}{\lambda'}$. In Fig. 45, the muon spin relaxation rate, $\lambda = \frac{1}{t_{1/2}}$, is shown for different applied pressures. The critical temperature, determined from the peak of the relaxation rate versus temperature plot, decreases systematically with increasing pressure.

In Fig. 46, we plot T_1 versus the inverse temperature. For each pressure, T_1 shows an approximately linear dependence on the inverse temperature. Our sample proved to be rather small for muon measurements under pressure, giving a small asymmetry. The combination of the uncertain background, used as a fit parameter, and the small asymmetry could introduce error in our determination of T_1.

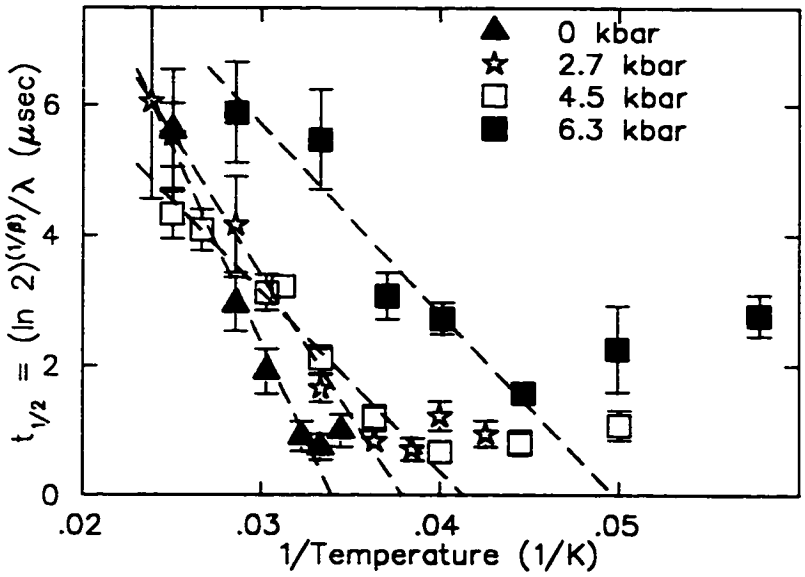

Figure 46: Relaxation time, T_1, of the muon spins in the MnSi sample as a function of the inverse temperature, under zero and applied pressures of 2.7, 4.5 and 6.3 kbar.

In Fig. 47, we show the evolution of the slope of the T_1 versus $\frac{1}{T}$ plot as a function of the applied pressure. The theory predicts a scaling of the slope with the critical temperature. The plot shows the reduction of the slope as the pressure is increased, except for the 6.3 kbar data. This inconsistency may be due to the fitting procedure. For the 6.3 kbar data, we extended the background interval from 400 nsec to 800 nsec, which may change our results to some extent.

We could approximately determine the precession frequency of the muon spins at 5 K under zero and two other applied pressures. In Fig. 48, our results of the precession frequency are plotted together with the

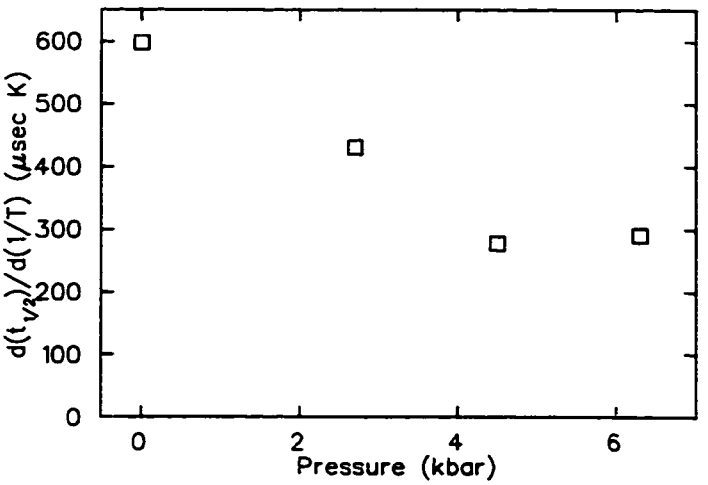

Figure 47: Slope of the T_1 versus the inverse temperature plot in the paramagnetic state, at ambient pressure and applied pressures of 2.7 kbar, 4.5 kbar and 6.3 kbar.

NMR resonance frequency of ^{29}Si at 1.4 K obtained by C. Thessieu and his collaborators [22]. The NMR results have been scaled so that the resonance frequency equals the μSR result under zero applied pressure. Consistent with NMR results, we see a systematic weak reduction of the precession frequency with pressure.

In conclusion, the data seems to show a linear dependence of the relaxation time with inverse temperature. However, it was premature to make solid conclusions regarding the behavior of the MnSi compound under pressure due to the spread in critical temperatures, limited quality of our data, and limited region of applied pressure.

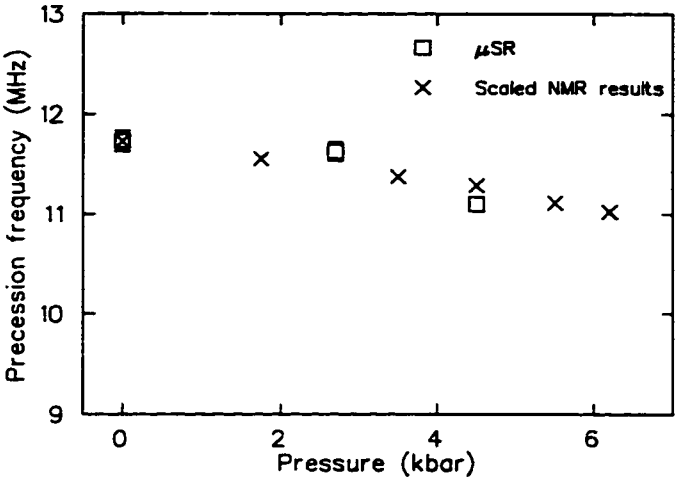

Figure 48: Precession frequency of the muon spins as a function of the applied pressure in the MnSi sample, together with NMR results of the resonance frequency of ^{29}Si scaled to the muon precession frequency at zero pressure.

7.2 Measurements under pressure at TRIUMF

We continued the experiments under pressure at TRIUMF. This time we used a larger single crystal of MnSi, kindly provided by Dr. Gen Shirane (Brookhaven National Laboratory). The use of single crystal specimens in μSR would assure homogeneity of the applied pressure, while powder specimens could be subject to some inhomogeneity of pressure.

In the ordered phase, we measured the muon precession frequency under zero magnetic field. To fit the data we performed a very careful background subtraction. Usually, the background is considered to be constant and the spikes appearing with the periodicity of the cyclotron

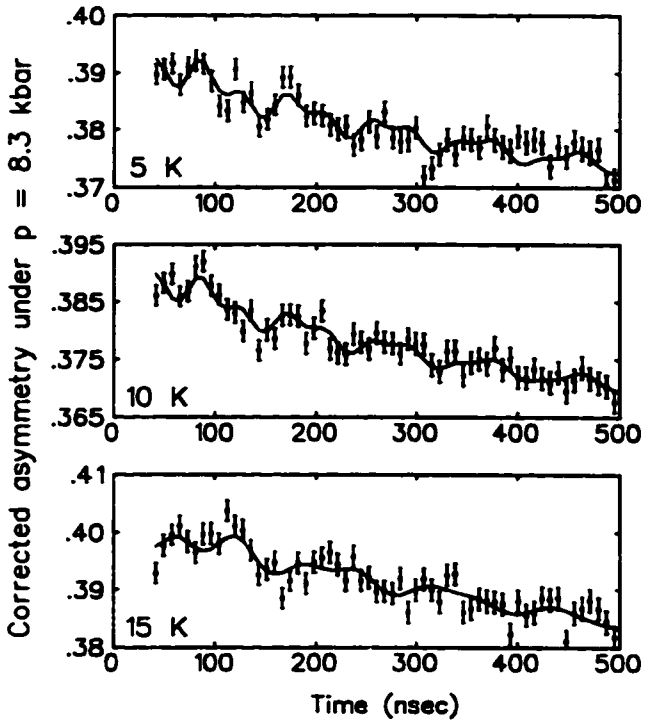

Figure 49: Evolution of the precession signal under 8.3 kbar as the temperature is increased. The corrected asymmetry is plot at 5 K, 10 K and 15 K, together with a fit to the data. Two precession frequencies could be distinguished. The amplitudes of the precession signals were kept constant for all temperatures.

(42 nsec) are ignored. To extract the data, we fit the background to a parabolical function having this periodicity. The data at 5 K, 10 K, and 15 K are shown in Fig. 49, after performing the background subtraction. We distinguished two frequencies at all temperatures. At 5 K, the amplitudes of the lower and higher frequency signals were 0.00195 and 0.0028, respectively, and we kept these values fixed while fitting the rest of the data.

Figure 50 shows our results for the precession frequency. The pre-

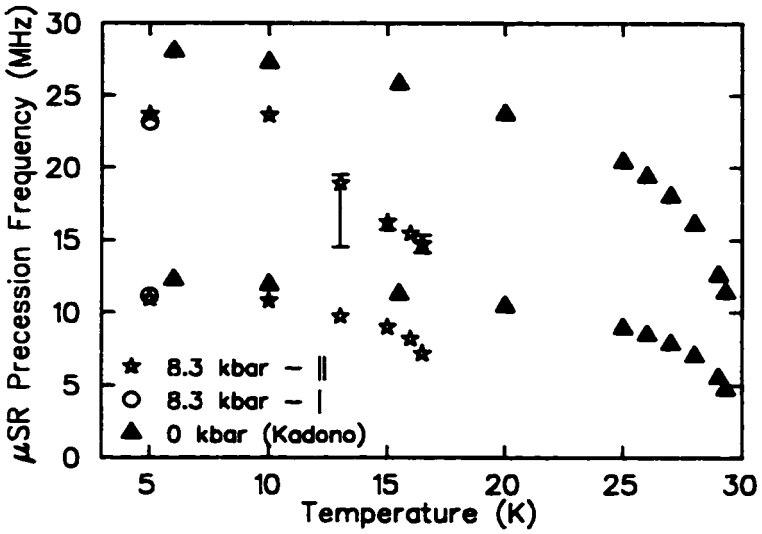

Figure 50: The precession frequency of the muon spins in MnSi under an applied pressure of 8.3 kbar is compared with data taken by Dr. Kadono and his collaborators [18] on MnSi at ambient pressure. The open circles represent the precession frequencies measured at a previous time. The agreement shows that the pressure did not change between the times of the measurements.

cession disappears completely at 17 K, which we consider to be T_c. The results for the higher frequency have a large systematic error due to limited statistics and small sample signal compared to the large background from the pressure cell. The ratio of the amplitudes is not relevant because of the same reason. The temperature dependence of the lower frequency is very similar with the temperature dependence of the precession frequency at ambient pressure obtained by Dr. Kadono and his collaborators [18]. This is a confirmation of the validity of our results.

In Fig. 51, we plot our results of the lower frequency under 8.3 kbar

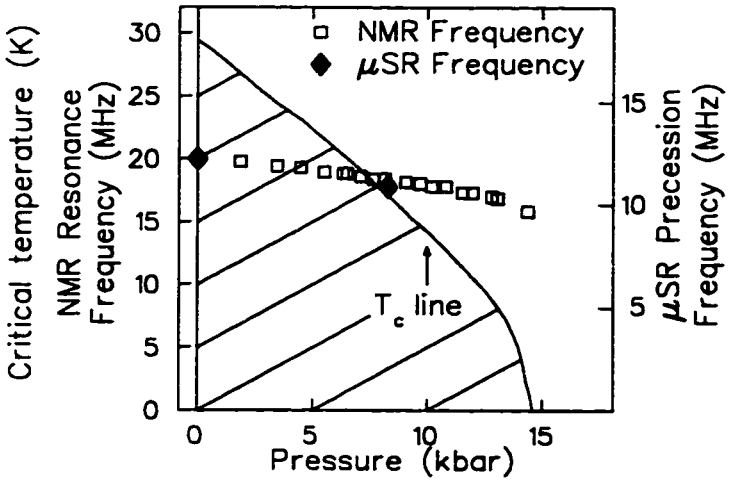

Figure 51: Pressure dependence of the NMR frequency and T_c [22] in MnSi. The present μSR result at 5 K is plotted with the rhombic symbol together with the lowest temperature precession frequency obtained by Kadono *et al.* [18].

at $T = 5$ K together with the value at ambient pressure [18] and the ^{29}Si NMR results for the pressure dependence of the magnetic moment [22]. Our results confirm the NMR results and show that the magnetic moment M_0 decreases much more slowly with increasing pressure, compared to the reduction of T_c. This behavior of the magnetic moment M_0 might be related to the first-order nature of the phase transition at p_c [19, 38].

In the paramagnetic phase, we measured the relaxation rate of muons due to electronic spin fluctuations. The application of a 61.3 G longitudinal field suppresses any contribution from the nuclear dipoles. After the background subtraction, the data of the paramagnetic state

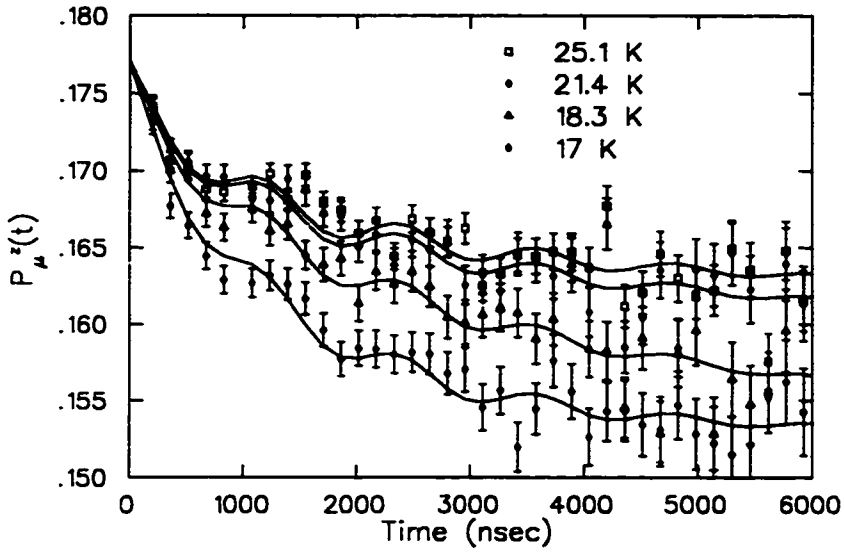

Figure 52: The muon spins polarization function of MnSi under an applied pressure of 8.3 kbar at 20.2, 18.3, 17.6 and 17 K. As the temperatures decreases towards $T_c = 17$ K, the relaxation becomes more pronounced.

has been fit with a simple exponential.

Figure 52 shows the corrected asymmetry at a few temperatures above T_c. The small amplitude oscillation is due to the background of the pressure cell. Under zero field, the pressure cell background could be fit with a Gaussian Kubo-Toyabe function with an amplitude of .154 and a field width of .334 μsec^{-1}. Under an applied field of 61.3 G the Gaussian Kubo-Toyabe function is strongly decoupled, the signal showing slight oscillations on top of a slowly decaying line. Added to the total signal, we identified in all runs a fast relaxing background of unknown origin, with an amplitude of 0.012. This could be fit with

a stretched exponential, $\exp(-(\lambda t)^{\beta})$, with $\lambda = 0.793\ \mu\text{sec}^{-1}$ and $\beta = 0.83$. Possibly, this background is due to the other components of the pressure cell, such as the piston.

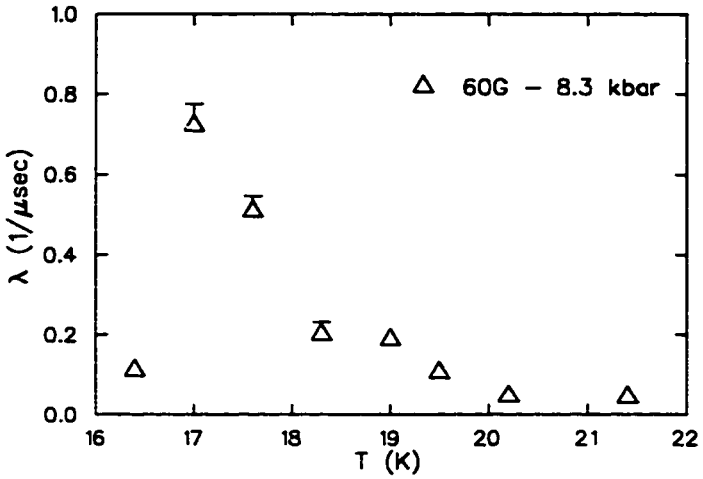

Figure 53: The relaxation rate of the muon spins in MnSi under an applied pressure of 8.3 kbar. λ takes its maximum value at $T_c = 17$ K.

The relaxation of the muon spins has a maximum at 17 K, where the precession in the ordered state disappears, as shown in Fig. 53. Our result of $T_c = 17$ K for 8.3 kbar is consistent with the pressure dependence of the critical temperature, determined previously by NMR and resistivity measurements.

Figure 54 shows the relaxation time $T_1 = \frac{1}{\lambda}$ as a function of the inverse temperature at 8.3 kbar and at ambient pressure. The plot of T_1 versus $1/T$ under applied pressure shows a pronounced curvature, espe-

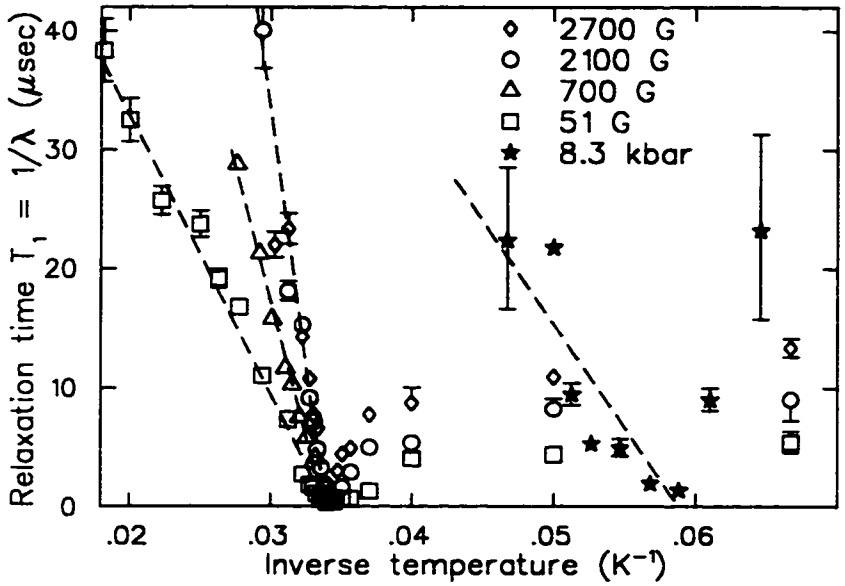

Figure 54: The relaxation time versus inverse temperature plot under 8.3 kbar is compared with the similar plot at ambient pressure under various applied magnetic fields. Under applied pressure the plot shows a pronounced curvature, as an indication of the system approaching the quantum critical point at p_c.

cially when compared with the similar plot at ambient pressure. This might be related to the MnSi system approaching the quantum critical point of the magnetic - nonmagnetic transition. As stated previously, for the very itinerant systems, one expects the small wave-vector and low energy spin fluctuations to contribute more significantly to the macroscopic properties of the system. The magnetic susceptibility departs from the Curie-Weiss law as the system becomes more itinerant. This could determine the nonlinearity of the T_1 versus $1/T$ plot at 8.3 kbar.

The success of this first μSR experiment on MnSi at 8.3 kbar opens the path for further measurements of MnSi under applied pressures, to improve our understanding of the behavior of the system close to the quantum criticality at p_c.

8 Conclusions

In conclusion, we presented new sets of μSR measurements on MnSi and elucidated the effect of the applied field on the critical behavior observed via the relaxation rate $1/T_1$. This emphasizes the limits of applicability of the SCR theory for weak ferromagnets in the case of the MnSi system and the need to account for the helical nature of the magnetic structure.

We also found near T_c a departure of $1/T_1$ from the linear behavior $T_1T \propto (T-T_c)$. This is a first μSR experiment to prove the predictions of the SCR theory for the relaxation time of the muon spins close to the critical temperature. We would like to perform more experiments using various systems to conclude on this subject.

We extended the μSR measurements by performing μSR on MnSi under applied pressure. We confirmed the very small pressure dependence of the magnetic moment in the ordered phase. We also obtained evidence for the departure of the $1/T_1$ from the relationship $T_1T \propto (T - T_c)$ in the critical region. More experiments on MnSi under pressure are desirable to consistently study the system near the

ferromagnetic to paramagnetic crossover.

References

[1] T. Moriya, Spin Fluctuations in Itinerant Electron Magnetism, Springer Series in Solid State Sciences.

[2] C. Pfleiderer, M. Uhlarz, S.M. Hayden, R. Vollmer *et al*, Nature **412**, 58 (2001).

[3] P. Langevin, J. Phys. (Paris) **4**, 678 (1905); Ann. Chym. Phys. **5**, 70 (1905).

[4] P. Weiss, J. Phys. Radium **6**, 661 (1907).

[5] J.H. Van Vleck, Theory of Electric and Magnetic Susceptibilities (Oxford Univ. Press. Oxford, 1932).

[6] W. Heisenberg, Z. Phys. **49**, 619 (1928).

[7] Y. Takahashi, J. Phys. Soc. Japan **55**, 3553 (1986).

[8] P.R. Rhodes, E.R. Wohlfarth: Proc. R. Soc. (London) **273**, 247 (1963).

[9] E. Wigner, Phys. Rev. **46**, 1002 (1934); Trans. Faraday Soc. **34**, 678 (1938).

[10] J.C. Slater, Phys. Rev. **49**, 537, 931 (1936).

[11] S. Doniach, Proc. Phys. Soc. **91**, 86 (1967) **56**, (Springer,Heidelberg, 1985).

[12] Y. Ishikawa, K. Tajima, D. Bloch, M. Roth, Solid State Commun. **19**, 525 (1976).

[13] Y. Ishikawa, T. Komatsubara, and D. Bloch, Physica **86-88** B, 401 (1977).

[14] E. Fawcett, J.P. Maita, J.H. Vernick, Int. J. Magnetism **1**, 29 (1970).

[15] H. Yasuoka, V. Jaccarino, R.C. Sherwood, J.H. Vernick, J. Phys. Soc. Japan **44**, 842 (1978).

[16] Y. Ishikawa, Y. Noda, Y.J. Uemura *et al*, Phys. Rev. B **31**, 5884 (1985).

[17] R. Hayano, Y.J. Uemura, J. Imazato *et al* J. Phys. Soc. Japan **49**, 1773 (1980).

[18] R. Kadono, T. Matsuzaki, T. Yamazaki, S.R. Kreitzman, J.H. Brewer, Phys. Rev. B **42**, 6515 (1990).

[19] C. Pfleiderer, G.J. McMullan, S.R. Julian, G.G. Lonzarich, Phys. Rev. B **55**, 8330 (1997).

[20] C. Thessieu, K. Ishida, Y. Kitaoka *et al*, J. Magn. Magn. Mater **177-181**, 609 (1998).

[21] C. Thessieu, K. Kamishima, T. Goto *et al*, J. Phys. Soc. Japan **67**, 3605 (1998).

[22] C. Thessieu, Y. Kitaoka, K. Asayama, Physica B **259-261**, 847 (1999).

[23] M. Takigawa, H. Yasuoka, Y.J. Uemura *et al*, J. Phys. Soc. Japan **49**, 1760 (1980).

[24] R. Kadono, J.H. Brewer, K. Chow *et al*, Phys. Rev. B **48**, 16803 (1993).

[25] A. Ishigaki, T. Moriya, Journal of the Physical Society of Japan **65**, 3402 (1996).

[26] M. Kontani, T. Hioki, Y. Masuda, Solid State Commun. **18**, 1251 (1975); Physica **86** B, 399 (1977).

[27] Y. Takahashi, T. Moriya, J. Phys. Soc. Jpn. **52**, 4342 (1983).

[28] A. Ishigaki, T. Moriya, J. Phys. Soc. Jpn. **67**, 3924-3935 (1998).

[29] O. Nakanishi, A. Yanase, A. Hasegawa, Solid State Commun. **35**, 995 (1980).

[30] M. Ishida, Y. Endoh, Y. Ishikawa, S. Mitsuda, and M. Tanaka (private communication).

[31] G. Shirane, R. Cowley, C. Majkrzak, Phys. Rev. B **28**, 6251 (1983).

[32] B. Roessli, P. Boni, W.E. Fischer, and Y. Endoh, Phys. Rev. Lett. **88**, (2002).

[33] K. Makoshi and T. Moriya, J. Phys. Soc. Japan **44**, 80 (1978).

[34] K. Nakayama and T. Moriya, J. Phys. Soc. Japan **56**, 2918 (1987).

[35] A. Buzdin, Y. Meurdesoif, JETP Lett. **65**, 814 (1997).

[36] R.S. Hayano, Y.J. Uemura, J. Imazato *et al*, Phys. Rev. B **20**, 850 (1979).

[37] A. Schenck, Muon Spin Rotation Spectroscopy Principles and Applications in Solid State Physics, (Adam Hilger Ltd 1985).

[38] C. Thessieu, K. Ishida, Y. Kitaoka, J. Magn. Magn. Mater, **177**, 609 (1998).